Local retinoic acid directs emergence of the extraocular muscle functional unit

Glenda Comai[1,#], Marketa Tesarova[2], Valerie Dupé[3], Muriel Rhinn[4], Pedro Vallecillo Garcia[5], Fabio da Silva[6,7], Betty Feret[4], Katherine Exelby[8], Pascal Dollé[4], Leif Carlsson[9], Brian Pryce[10], Francois Spitz[11], Sigmar Stricker[5], Tomas Zikmund[2], Jozef Kaiser[2], James Briscoe[8], Andreas Schedl[6], Norbert B. Ghyselinck[4], Ronen Schweitzer[10] and Shahragim Tajbakhsh[1,#]

1 Stem Cells & Development Unit, UMR CNRS 3738, Institut Pasteur, Paris, France
2 Central European Institute of Technology, Brno University of Technology, Brno, Czech Republic
3 Université de Rennes, CNRS, IGDR, Rennes, France
4 IGBMC-Institut de Génétique et de Biologie Moleculaire et Cellulaire, Illkirch, France
5 Institute for Chemistry and Biochemistry, Freie Universität Berlin, D-14195 Berlin, Germany
6 Université Côte d'Azur, INSERM, CNRS, iBV, Nice, France
7 Division of Molecular Embryology, German Cancer Research Center (DKFZ), Heidelberg
8 The Francis Crick Institute, London, NW1 1AT, United Kingdom
9 Umea Center for Molecular Medicine, Umea University, Umea, Sweden
10 Research Division, Shriners Hospital for Children, Portland, OR 97209, USA
11 Genomics of Animal Development Unit, Institut Pasteur, Paris, France
Authors for correspondance

ABSTRACT

Coordinated development of muscles, tendons, and their attachment sites ensures emergence of functional musculoskeletal units that are adapted to diverse anatomical demands among different species. How these different tissues are patterned and functionally assembled during embryogenesis is poorly understood. Here, we investigated the morphogenesis of extraocular muscles (EOMs), an evolutionary conserved cranial muscle group that is crucial for the coordinated movement of the eyeballs and for visual acuity. By means of lineage analysis, we redefined the cellular origins of periocular connective tissues interacting with the EOMs, which do not arise exclusively from neural crest mesenchyme as previously thought. Using 3D imaging approaches, we established an integrative blueprint for the EOM functional unit. By doing so, we identified a developmental time window where individual EOMs emerge from a unique muscle anlage and establish insertions in the sclera, which sets these muscles apart from classical muscle-to-bone type of insertions. Further, we demonstrate that the eyeballs are a source of diffusible retinoic acid that allow their targeting by the EOMs in a temporal and dose dependent manner. Using genetically modified mice and inhibitor treatments, we find that endogenous local variations in the concentration of retinoids contribute to the establishment of tendon condensations and attachment sites that precede the initiation of muscle patterning. Collectively, our results highlight how global and site-specific programs are deployed for the assembly of muscle functional units with precise definition of muscle shapes and topographical wiring of their tendon attachments.

INTRODUCTION

Acquisition of shape and pattern during development depends on the orchestrated crosstalk between a variety of tissues and cell types. While significant knowledge on the mechanisms of differentiation and patterning within individual tissues has been attained, much less is known on how patterning of different adjacent tissues is integrated. The vertebrate musculoskeletal system serves as an ideal model to study these processes as different tissues including muscle, tendon and their attachments need to be articulated in three-dimensions (3D) for proper function (Hasson, 2011; Huang, 2017).

Among the craniofacial muscles, the morphological configuration of the extraocular muscles (EOMs) has been a longstanding challenge in comparative anatomy and evolutionary biology. Besides specialized adaptations, the basic EOM pattern is shared among all vertebrate classes (Noden and Francis-West, 2006; Suzuki et al., 2016; Young, 2008) and includes 4 recti muscles (the superior rectus, the medial rectus, the inferior rectus, and the lateral rectus) and two oblique muscles (superior oblique and inferior oblique) for movement of the eyeball. Most vertebrates have also accessory ocular muscles involved in protecting the cornea (Noden and Francis-West, 2006; Spencer and Porter, 2006): the retractor bulbi, which serves to retract the eye in several groups of vertebrates and the levator palpabrae superioris, which is not directly associated with the eyeball but controls eyelid elevation in mammalian species. As such, the EOMs constitute an archetypal and autonomous functional unit for the study of how muscles, tendons and tendon attachments are integrated with the development of the eyeball, their target organ.

Craniofacial muscles are derived from cranial paraxial and prechordal head mesoderm (Noden and Francis-West, 2006; Ziermann et al., 2018) and the corresponding connective tissues, i.e. tendons, bones and cartilages and muscle connective tissue surrounding myofibres, were reported to be derived from cranial neural crest cells (NCC) (Nassari et al., 2017; Ziermann et al., 2018). Although early myogenesis is NCC-independent, NCC later regulate the differentiation and segregation of muscle precursors, dictate the pattern of muscle fiber alignment, and that of associated skeletal and tendon structures (Bohnsack et al., 2011; Ericsson et al., 2004; Noden, 1983b; Rinon et al., 2007; Tokita and Schneider, 2009; von Scheven et al., 2006). Moreover, studies of mouse mutants in which several genes were deleted in NCC cells have explicitly demonstrated their non-cell autonomous role in muscle morphogenesis at the level of the jaw (McGurk et al., 2017; Rinon et al., 2007; Shimizu et al., 2018), extraocular (Evans and Gage, 2005; Heude et al., 2015) and somitic-derived tongue muscles (Iwata et al., 2013). However, the full series of events driving morphogenesis of craniofacial musculoskeletal functional units is to date unexplored, probably due to the anatomical complexity of their configuration in the head.

Understanding the developmental mechanisms that allow musculoskeletal connectivity is essential to understand their anatomical diversification during the evolution of the vertebrate head. Yet, proximate factors that allow the coordinated emergence of the individual muscle masses with that of their tendons and attachment sites are poorly defined.

To-date, much of the work on the tissue interdependency during musculosketal development has been done in the developing limb. Lateral plate mesodem derived connective tissue cells and tendon primordia establish a pre-pattern and restrict the locations where limb muscle progenitors proliferate and differentiate (Kardon, 1998; Kardon et al., 2003) prior to segregation (splitting) into individual muscle masses by several extrinsically controlled mechanisms (Hasson, 2011; Sefton and Kardon, 2019). Limb tendons are initially established independently of muscle, but their later development is modular, and depend on muscle or cartilage according to their location in the limb (Huang, 2017). Finally, generation of bone superstructures enable anchoring of muscles via tendons to the skeleton. Bone superstructures are initiated independently of muscle, by a unique set of progenitors that co-express SOX9 and Scleraxis (Scx) (Blitz et al., 2013; Blitz et al., 2009; Sugimoto et al., 2013), but remarkably, muscle and superstructure patterning seem to be regulated in a coordinated manner (Colasanto et al., 2016; Swinehart et al., 2013). However, given the striking differences in gene regulatory networks governing cranial muscle development (Diogo et al., 2015; Sambasivan et al., 2011), as well as the diverse embryological origins of connective tissue cells in the head (Nassari et al., 2017; Ziermann et al., 2018), it is unclear if this established logic of musculoskeletal integration is conserved in the head and for muscles that do not operate with muscle-to-bone attachments such as the EOMs.

It has been proposed that the developing central nervous system, sensory organs, pharyngeal endoderm and surface ectoderm provide spatial patterning cues to cranial connective tissue precursors (Noden and Francis-West, 2006; Ziermann et al., 2018). In this context, all-trans retinoic acid (ATRA), the biologically active metabolite of retinol (vitamin A), is a critical morphogen with widespread roles in craniofacial development (Gitton et al., 2010; Rhinn and Dolle, 2012). ATRA acts as a ligand for nuclear retinoic acid receptors (RARs), which are ligand-dependent transcriptional regulators that work as heterodimers with retinoid X receptors (RXRs) (Cunningham and Duester, 2015; Rhinn and Dolle, 2012). ATRA is synthetized from retinol through two oxidation steps by specific retinol/alcohol dehydrogenases (RDH/ADH) and retinaldehyde dehydrogenases (ALDH1A1, ALDH1A2 and ALDH1A3) and catabolized into hydroxylated derivatives by enzymes of the cytochrome P450 subfamily (CYP26s) (Cunningham and Duester, 2015; Rhinn and Dolle, 2012). ATRA was shown to be critical for early eye development in several species (Bohnsack et al., 2012; Harding and Moosajee, 2019; See et al., 2008), where the enzymes responsible of ATRA metabolism are expressed in the early retina with tight spatiotemporal patterns (Cvekl and

128 Wang, 2009). Several studies have demostrated that through production of RA, the
129 developing eye acts as a signaling center nucleating anterior segment morphogenesis, with
130 the transcription factor *Pitx2* as the potential major downstream effector in periocular NCC
131 (Bohnsack et al., 2012; Matt et al., 2005; Matt et al., 2008; Molotkov et al., 2006). However,
132 whether ATRA is required for morphogenesis of the adjacent EOMs and associated
133 connective tissues remains unexplored.

134 Here, by a combination of 3D-mesoscopic imaging approaches, we present the first
135 integrative blueprint for morphogenesis of the EOM functional unit. We provide genetic
136 evidence for the existence of a retinoic acid signaling module that coordinates the
137 emergence of individual EOMs, their tendons and insertion sites. We show that the action of
138 retinoic acid signaling in muscle patterning is mainly non-cell autonomous, through its action
139 on the neural crest-derived periocular mesenchyme. Furthermore, we characterise the
140 dynamics of EOM-tendon insertion sites, which are impaired upon ATRA-deficiency. Overall,
141 our results show that in spite of the distinct embryological origins of these tissues in the
142 head, interactions between muscles, tendons and their attachments are similar to those
143 observed in the limb, yet they exhibit specifc hallmarks that are characteristic of this
144 anatomical location. This includes regionalized apoptotic foci that presage tendon attachment
145 sites in a context that is distinct from the canonical tendon to bone configuration.
146

147 **Results**

148 **Genetic fate mapping of mouse periocular tissues**

149 To investigate the morphogenesis of the EOMs in the mouse, we focused first on
150 adjacent tissues whose development should be coordinated with that of the EOMs. The
151 periocular mesenchyme (POM) is a heterogeneous cell population surrounding the optic cup
152 that gives rise to specialized structures of the anterior segment of the eye and connective
153 tissues associated with the EOMs (Williams and Bohnsack, 2015). With exception of the
154 EOMs and endothelial lining of ocular blood vessels (choroid), all connective tissues of the
155 POM (cartilage, muscle connective tissue, tendons), were reported to be derived from NCC
156 in zebrafish, chicken and mouse embryos (Couly et al., 1992; Creuzet et al., 2005; Gage et
157 al., 2005; Grenier et al., 2009; Johnston et al., 1979; Noden, 1983a). However, the extent of
158 the POM in relation to its different cell populations, has not been fully assessed. Thus, we
159 investigated the expression pattern of PITX2, a well established marker of both the POM and
160 EOM progenitors (Gage et al., 2005), *Scx*, a tendon progenitor marker (Schweitzer et al.,
161 2001) and SOX9, which is expressed in NCC and required for determination of the
162 chondrogenic lineage (Mori-Akiyama et al., 2003). We simultaneously traced the contribution
163 of different embryonic populations using $Mesp1^{Cre};R26^{tdTomato}$ and $Wnt1^{Cre};R26^{tdTomato}$ mice

that label the mesodermal and NCC derivatives (Danielian et al., 1998; Saga et al., 1999) in combination with the *Tg:Scx-GFP* transgenic line (Pryce et al., 2007).

Coronal sections at the level of the eye at E13.5 showed that *Scx-GFP*, SOX9 and PITX2 expression delimited a triangular area of cells medial to the eyeball encompasing the EOMs (dotted lines, Fig 1A-D), however, with variable intensities along the medio-lateral axis. SOX9 and PITX2 were more strongly expressed laterally between the retina and ectoderm, where the EOM tendons insert. The *Scx-GFP* reporter labelled the future EOM tendons and also muscle connective tissue as described for other muscles (Deries et al., 2010). As expected, EOM tendons and muscle connective tissue at the insertion level were of NCC origin ($Wnt1^{Cre};R26^{tdTomato}$, Fig 1A-D). Surprisingly, we found that lineage contributions differed in dorsal sections. The future Annulus of Zinn, the tendinous ring from which the recti muscles originate at the base of the skull (Spencer and Porter, 2006), as well as the muscle connective tissue at this level, were of mesodermal origin ($Mesp1^{Cre};R26^{tdTomato}$, Fig 1E-H), although they also co-expressed *Scx-GFP*, SOX9 and PITX2 at this stage. The dual mesoderm/NCC contribution to POM connective tissues was observed from E11.5 (not shown) to E17.5 (Suppl Fig 1A-F). These findings indicate that the EOMs develop in close association with connective tissues of two distinct embryonic origins: neural crest laterally (at the EOM insertion level) and mesoderm medially (at the EOM origin level).

Development of the EOMs and their insertions overlap spatio-temporally

Patterning of the EOMs and their insertions has been largely disregarded due to their complex anatomy, which is difficult to interpret from tissue sections alone. Therefore, we established an imaging pipeline that includes whole mount immunofluorescence (WMIF) of the periocular region, tissue clearing, confocal microscopy and reconstructions of the obtained images into 3D objects. To visualize the developing EOM we used MYOD/MYOG/Desmin as myogenic commitment and differentiation markers and MF20 to label myofibers (Fig 2A-C', Video 1). At E11.75, the EOMs were present as a single anlage (Fig 2A-A') medial to the eyeball. By E12.5, the EOM anlage split towards the POM-ring into the submasses corresponding to the future four recti, two oblique muscles and the accesory retractor bulbi muscle (Fig 2B-B'). Fully separated muscle subsets were evident by E13.5 (Fig 2C-C'). Thus, we conclude that EOM patterning in the mouse occurs by splitting from a single anlage with major morphogenetic changes taking place between E11.75 and E12.5.

The EOMs insert into the sclera, a dense fibrous layer derived from the POM. Foci of cell death in the POM were suggested to label the tendon attachment positions of the 4 recti muscles (Sulik et al., 2001). Thus, to better understand the establishment of the EOM insertions in the POM within the time window of EOM patterning, we performed whole mount

201 immunostaining for the POM marker PITX2 and LysoTracker Red staining to detect
202 programmed cell death on live embryos (Fogel et al., 2012) (Fig 2D,E). WMIF for the PITX2
203 at E11.75 revealed a ring of PITX2^{high} cells immediately adjacent to the retinal pigmented
204 epithelium (RPE) (POM-ring) that formed a continuum with PITX2^{low} cells extending towards
205 the base of the EOM anlage (medial-POM) (Fig 2D). Lysotracker Red staining revealed a
206 highly dynamic pattern in the POM-ring, where four foci were present at E11.75 at the
207 horizons of the eye, which regressed from E12.5 onwards (Fig 2E). To confirm that the
208 apoptotic foci define tendon attachment positions in the POM, we performed whole mount
209 imunostaining for EOM progenitors and GFP (*Tg:SCX-GFP*) on Lysotracker stained
210 embryos. Surprisingly, we observed that even before muscle splitting initiated, *Scx-GFP*+
211 condensations bridged the edges of the EOM anlage and the four Lysotracker+ foci in the
212 POM (E11.75, Video 2), presaging the locales of the future individual muscles (E12.5, Video
213 3).
214 To examine the EOM insertions with higher resolution, we immunostained
215 *Wnt1^{Cre};R26^{tdTomato};Scx-GFP* coronal sections with POM markers (Fig 2F-N). At E12, PITX2
216 and SOX9 showed high expression in the lateral POM at the insertion site, while *Scx-GFP*
217 was mostly expressed in a salt and pepper pattern at this level (Fig 2G-I). Where cells
218 appeared more compact, as assessed by SOX9 and PITX2 staining, the Tomato staining
219 appeared punctate (Fig 2F), reminiscent of apoptotic cells. Cell death was confirmed by
220 LysoTracker Red and TUNEL staining on adjacent sections (Fig 2J, J'). By E13.5, PITX2
221 continued to mark a large periocular region, but SOX9 and *Scx-GFP* expression patterns
222 were segregated and apoptotic foci undetectable (Fig 2K-N). Sox9 was expressed more
223 laterally in a condensed group of cells probably representing the lateral tendon attachment
224 points (Fig 2M), preceded medially by strong *Scx-GFP* staining at the tendon tips (Fig 2N).
225 By E14.5, lateral EOM tendons expressed *Scx-GFP*, Tenascin and also PITX2 (Fig 2P-R,
226 Suppl Fig 2A-H). At this stage, expression of SOX9 and PITX2 were donwregulated in the
227 POM and reduced to the thin scleral layer (Fig 2R, S, Suppl Fig 2E-L). Altogether, these
228 results show that patterning of the EOMs, their tendons and insertion sites overlap spatio-
229 temporally and thus might be regulated in a coordinated manner. Moreover, similarly to other
230 locations in the body, *Scx* and SOX9 show complementary patterns at the EOM insertion
231 site, but additional specifc hallmarks, notably the presence of apoptotic foci and PITX2
232 expression, seem to be characteristic of this site.
233
234 **Abnormal EOM morphogenesis in mutants with ocular malformations**
235 To obtain further insights into the development of the EOM functional unit, we next
236 focused on the role of the target organ, the eyeball, on EOM patterning. To this end, we
237 performed micro-computed tomography (micro-CT) scans in mouse mutants with a spectrum

238 of ocular perturbations. First, we analyzed *Pax6*$^{Sey/Sey}$ embryos, which are anophthalmic
239 where eye development is arrested at the optic vesicle stage (Grindley et al., 1995; Kaufman
240 et al., 1995; Roberts, 1967). In heterozygote embryos, EOM patterning proceeded as in
241 wildtype controls, where 4 recti and 2 oblique muscles were identifiable by E13.5 (Fig 3A, B).
242 In contrast, *Pax6*$^{Sey/Sey}$ mutant EOMs appeared as a unique sheet of tissue on top of a
243 rudimentary optic vesicle (Fig 3C). Given that Pax6 is expressed in the optic vesicle, giving
244 rise to the retina and RPE, as well as in the overlying ectoderm that forms the lens and
245 cornea (Grindley et al., 1995), but not in the EOMs, these observations suggest a non-cell
246 autonomous role in EOM patterning. Similarly, in *Lhx2*^{Cre}*;Lhx2*$^{fl/fl}$ embryos, where inactivation
247 of the *Lhx2* gene in eye committed progenitor cells leds to a degeneration of the optic vesicle
248 at E11.5 (Hagglund et al., 2011), EOM patterning was severely affected and few EOM
249 submasses could be observed (Suppl Fig 3A-B'). Finally, in cyclopic embryos resulting from
250 inversion of Shh regulatory regions, EOMs underwent splitting and projected towards the
251 centrally located ectopic eye, although with an abnormal 3D arrangement as reported for
252 human cyclopia conditions (Suppl Fig 3C-C'') (Ziermann et al., 2018). Together with previous
253 studies where surgical removal of the developing eye results in smaller EOMs with limited
254 spatial organization (Bohnsack et al., 2011; Twitty, 1932; von Scheven et al., 2006), our
255 observations reinforce the notion that the eye is not only a target organ for muscle insertion,
256 but it plays a critical role as an organizer of EOM patterning. However, as severe eye defects
257 are associated with abnormal migration of NCC to the periocular region (Langenberg et al.,
258 2008; Matsuo et al., 1993), it is difficult to pinpoint the underlying cause of the observed EOM
259 phenotypes. Thus, we decided to assess directly whether the developing eye could act as a
260 source of molecular signals to induce the geometrically complex EOM pattern and that of
261 their associated connective tissues.
262
263 **Muscle patterning depends on retinoic acid signaling of neural origin**
264 To study the role of target organ derived cues in EOM patterning, we investigated the
265 role of retinoic acid signaling, which plays multiple paracrine roles during embryonic eye
266 development (Cvekl and Wang, 2009). As ALDH1A1-3 are the rate-limiting enzymes in the
267 production of ATRA (Duester, 2009), we characterised their expression in the periocular
268 region at the time of EOM patterning. Between E10.5 and E12.5, *Aldh1a1* was expressed
269 strongly in the dorsal retina, lens and corneal ectoderm (Suppl Fig 4A), *Aldh1a2* was
270 expressed in the temporal mesenchyme (Suppl Fig 4A-A"), and *Aldh1a3* was mostly
271 restricted to the ventral retina and corneal ectoderm (Fig 4A, Suppl Fig 4A) (Matt et al., 2005;
272 Molotkov et al., 2006). Interestingly, ALDH1A3 was the only retinaldehyde dehydrogenase
273 protein detected in the RPE and optic stalk/optic nerve between E10.5-E12.5 and thus
274 centrally positioned with respect to EOM development (Fig 4A). To target the retinoic

signaling pathway (Fig 4B), we used *Aldh1a3*$^{-/-}$ (Dupe et al., 2003) and *Rdh10*$^{-/-}$ (Rhinn et al., 2011) mutants. We also administered the BMS493 inhibitor (pan-RAR inverse agonist) to pregnant females every 10-12h between E10.5-E11.75, i.e. preceeding the initiation of muscle splitting (Fig 2A-C) and once NCC migration to the POM has finalized (Osumi-Yamashita et al., 1994; Serbedzija et al., 1992). Micro-CT analysis showed that *Aldh1a3*$^{-/-}$ and BMS493-treated embryos displayed eye ventralization and a shortened optic nerve when compared to controls (Suppl Fig 4B), but they retained the overall organization of the nasal capsule and orbit (Suppl Fig 4C). Ventral and lateral views of the 3D-reconstructed EOMs (Fig 4C-E), showed that *Aldh1a3*$^{-/-}$ and BMS493-treated embryos lacked the standard 3D arrangement of 4 recti and 2 oblique muscles observed at E13.5 in control embryos. Nevertheless, in all cases EOMs originated medially from the hypochiasmatic cartilages of the presphenoid bone, indicating that the overall orientation of the EOMs was preserved (Fig 4D'''). Thus, given that the EOMs are more affected at their insertion than their origin level upon ATRA deficiency, this finding suggests that EOM patterning is in part modular.

To analyze EOM and tendon patterning with higher resolution, we performed whole mount immunostainings for differentiated myofibres (MyHC) and tendon (Tenascin) (Fig 4F-H'). On medial and lateral views of 3D-reconstructed EOMs, only the retractor bulbi and superior rectus could be clearly identified among the non-segregated muscle fibres in *Aldh1a3*$^{-/-}$ embryos (Fig 4G, G'). As expected from global invalidation of retinoic acid signaling, EOM perturbation was more severe in BMS493-treated embryos (Fig 4H, H'). The SO was absent, or continuous with the anterior part of the anlage, and the medial portion of the retractor bulbi was thicker and less clearly isolated from the rest of the anlage. In both conditions, Tenascin and *Scx-GFP*+ cells were present at the tips of the individual, though mispatterned, muscles at this stage (Fig 4G',H', Video 4). Analysis of *Aldh1a3*$^{-/-}$ and BMS493-treated embryos revealed on average a 26% reduction in the EOM volume compared to controls (Fig 4I). However, MyHC+ myofibres were present in *Aldh1a3*$^{-/-}$ and BMS493-treated embryos (Fig 4G,H), suggesting that EOM differentiation was not overtly affected in these conditions. Instead, these observations suggest that EOM fiber alignment and segregation is dependent on retinoic acid signaling.

As dose and temporal control are critical in the context of retinoic acid signaling (Chawla et al., 2016; Gitton et al., 2010; See et al., 2008), we performed other BMS493 injection regimes between E10.5 and E12.5 (Table 1). EOM patterning phenotypes categorised as strong or severe at E13.5 were only obtained when a E10.75 time point of injection (8PM of day E10.5) was included in the regime (experiment type I-III, Table 1, Suppl Fig 4D). Surprisingly, even a single injection at this time point resulted in strong phenotypes (experiment type IV, Table 1, Suppl Fig 4D), while exclusion of this timepoint (experiment type VI and V, Table 1, Suppl Fig 4D) resulted only in mild phenotypes at best. Therefore, we

312 identified an early and restricted temporal window where ATRA activity, prior to any sign of
313 muscle splitting, impacts correct muscle patterning 36-48 hours later. Given the critical action
314 of RDH10 in generating retinaldehyde, the intermediate metabolite in the biosynthesis of
315 ATRA, we examined EOM development in *Rdh10* mutant embryos. *Rdh10* is normally
316 expressed in the optic vesicle and RPE (Sandell et al., 2007), and in *Rdh10*$^{-/-}$ embryos, eyes
317 develop intracranially, close to the diencephalon with a very short ventral retina (Rhinn et al.,
318 2011). WMIF analysis of *Rdh10* mutant EOMs revealed that the anlage was specified, but
319 lacked any sign of segmentation, in agreement with an upstream role in ATRA synthesis
320 (Suppl Fig 4E,F). Taken together, our data show that retinoic acid signaling is essential for
321 the correct myofiber alignment and segregation of EOM masses in a dose and time
322 dependent manner.
323
324 **Muscle patterning is dependent on ATRA-responsive cells in the periocular**
325 **mesenchyme**
326 To track cells that are responsive to ATRA and responsible of EOM patterning we
327 used a novel retinoic acid transgenic reporter line (Schedl et al., unpublished) that comprises
328 three *RARE* elements from the *Rarb* gene fused to the *Hsp68* promoter driving expression of
329 a tamoxifen-inducible *Cre-ERT2* recombinase. By crossing this line with the *R26*^{mTmG} reporter
330 mice (Muzumdar et al., 2007) (Fig 5A, *Rare*^{CreERT2}*;R26*^{mTmG}), we permanently labelled ATRA-
331 responsive cells and their descendants with membrane GFP expression. We found a greater
332 amount of responsive cells in the periocular region when Tamoxifen was administered
333 between E9.75-E10.5 (Suppl Fig 5A-C). To assess if myogenic cells and the adjacent POM
334 respond to retinoic acid signaling, we scored the co-expression of GFP (reporter) and
335 myogenic markers (PAX7, MYOD, MYOG) in bulk cell preparations from the periocular
336 region. Notably, the great majority of reporter positive-responsive cells were not myogenic
337 and thus were part of periocular conective tissues (88% if induction at E9.75; 98% if
338 induction at E10.5) (Fig 5B,C). Upon induction of the reporter at E9.75, and analysis on
339 tissue sections and by WMIF at E11.75 and E12.5, we observed that the mesenchyme
340 around the optic nerve in close proximity to the developing EOMs was positive for the
341 reporter (Fig 5D-E',H). Interestingly, the overal number of POM GFP+ cells increased from
342 E11.75 to E12, which is the temporal window corresponding to EOM splitting (Fig 5D-E').
343 The SOX9+ POM-ring that includes the EOM attachments also had abundant numbers of
344 GFP+ cells (Fig 5F-G',H'). Finally, inactivation of downstream retinoic acid signaling with
345 BMS493, prior and subsequent to the induction of *Rare*^{CreERT2}*;R26*^{mTmG} mice with Tamoxifen
346 (Suppl Fig 5D), greatly reduced the responsiveness of the reporter in the POM compared to
347 non-treated controls and led to muscle mispatterning (Suppl Fig 5E-H, Videos 5 and 6).
348 Together, these results are in agreement with previous studies (Matt et al., 2005; Matt et al.,

349 2008; Molotkov et al., 2006) showing that despite a sophisticated pattern of ATRA
350 metabolism in the developing retina, retinoic acid signaling exerts its action mostly non-cell
351 autonomously, in the adjacent POM, and within a temporal window that is crucial for EOM
352 patterning.

353 Compound *Aldh1a1/Aldh1a3* mutants (Matt et al., 2005; Molotkov et al., 2006),
354 *Rarb/Rarg* mutants (Ghyselinck et al., 1997) and *Rarb/Rarg* NCC-specific mutants (Matt et
355 al., 2008) display similar phenotypes in the anterior segment of the eye and POM. These
356 findings have been attributed to the fact that ATRA synthesized by ALDH1A1 and ALDH1A3
357 in the neural retina activate RARB and RARG in the POM, which work as heterodimers with
358 RXRA (Kastner et al., 1994; Mori et al., 2001). To directly examine whether the role of
359 retinoic acid signaling in muscle patterning is driven non-cell autonomously, through the
360 action of RARB/RARG receptors in the NCC-derived POM, we performed WMIF for muscle
361 in *Wnt1*^{Cre};*Rarb*$^{fl/fl}$;*Rarg*$^{fl/fl}$ embryos. Accordingly, these NCC-*Rarb/Rarg* mutants showed
362 absence of muscle splitting (Fig 5I-J') as observed in *Rdh10*$^{-/-}$ embryos (Suppl Fig 4F).
363 Altogether, these data suggest that synthesis of ATRA from neural derivatives (retina, optic
364 nerve, RPE) at early stages (≈E10.5) is crucial for EOM patterning, through its action on
365 NCC-derived periocular connective tissues.
366

367 **Defective organization of the EOM insertions in retinoic acid signaling deficient**
368 **embryos**

369 To examine which connective tissue subpopulations, including the EOM insertions in
370 the POM, were affected by retinoic acid signaling deficiency, we assessed the distribution of
371 POM markers on tissue sections of *Aldh1a3*$^{-/-}$ and BMS493-treated embryos. Examination of
372 the distrubution of Collagen XII (Fig 6A-C'), a marker of the sclera and the presumptive
373 corneal epithelium (Oh et al., 1993), showed that ATRA-deficiency led to reduced expression
374 of Collagen XII at E12 at the level of the medial-POM which gives rise to the sclera (Fig 6B-
375 C, brackets, B'-C' insets). In addition, while PITX2 was expressed continuously in the entire
376 POM in controls (Fig 6D, dotted lines, D', inset), expression in the medial-POM was lost upon
377 ATRA-deficiency (Fig 6E-F, brackets, E',F', insets). This observation is in agreement with
378 *Pitx2* being a retinoic acid signaling target in the NCC-derived POM (Matt et al., 2005; Matt et
379 al., 2008; Molotkov et al., 2006) and the sclera being absent at fetal stages in *Rarb/Rarg*-
380 NCC mutants (Matt et al., 2008). Interestingly, POM organization was unaffected in
381 *Myf5*$^{nlacZ/nlacZ}$ mutants (Fig 6G, dotted lines, G', inset), where the initial EOM anlage forms but
382 myogenesis is aborted from E11.5 (Sambasivan et al., 2009). Thus, we conclude that
383 intrinsic organization of the POM is dependent on retinoic acid signaling but not on the
384 presence of myogenic cells.

To understand if the abnormal distribution of POM markers translates into EOM insertion defects, we examined the organization of the POM-ring in 3D in control, *Aldh1a3*$^{-/-}$ and BMS493-treated embryos. We systematically compared E11.75 and E12 embryos to visualize the organization of these tissues prior to, and during muscle splitting (Fig 2A-C). Control embryos showed the presence of partially overlapping SOX9 and PITX2 POM-ring domains, together with 4 apoptotic foci labelling the prospective tendon attachment points of the 4 recti muscles (Fig 6H-J, Suppl Fig 6A-C',E,F). As expected, ATRA-deficiency perturbed these patterns in a dose dependent manner. In lateral views of the head of *Aldh1a3*$^{-/-}$ embryos, SOX9 and PITX2 had narrower expression domains than controls, restricted to the anterior-dorsal and ventro-lateral eye quadrants (Fig 6K-L, Suppl Fig 6G,H). In BMS493-treated embryos, expression of SOX9 in the POM (Fig 6N, Suppl Fig 6I) and RPE (Suppl Fig 6D,D') was reduced to a minority of cells, and PITX2 expression was restricted ventro-laterally (Fig 6O, Suppl Fig 6J). Accordingly, the apoptotic foci were lost or disorganized in both cases of ATRA-deficiency with a single ventro-medial Lysotracker+ spot almost invariably present in both conditions (Fig 6M,P, Suppl Fig 6G-J). Finally, in medial views of the reconstructed 3D volume, we saw a continuum of PITX2 expression from the POM-ring to the medial-POM in control embryos (Suppl Fig 6N), while we noticed loss of medial-POM PITX2 expression in both cases of ATRA-deficiency (Suppl Fig 6O-P, blue arrowheads) as observed on tissue sections (Fig 6E',F', brackets). Thus, ATRA is required for the proper specification/organization of the medial POM and POM-ring.

As tendons were present at muscle tips in E13.5 *Aldh1a3*$^{-/-}$ and BMS493-treated embryos, but located ectopically with respect to a wild-type configuration (Fig 4F'-J'), we suspected that the initial 3D-organization of *Scx-GFP*+ tendon and connective tissue progenitors might also be affected. We performed WMIF for differentiated muscle (MyHC) and tendon (*Tg:SCX-GFP*) and segmented the reconstructed 3D volume. In control embryos at E12.5, *Scx-GFP*+ condensations projected from the tips of the future 4 recti muscles towards the POM-ring (Fig 6 Q,Q', Video 7), facing the 4 apoptotic foci (Fig 6J, Video 3). Moreover, *Scx-GFP*+ cells were also present in POM-muscle connective tissue presaging the final locales of the recti muscles (Fig 6T). In BMS493-treated embryos at E12, *Scx-GFP* expression was less organized and diffuse (Fig 6R,R', blue arrowhead) yet *Scx-GFP*+ condensations could be observed at the tips of ectopic muscle masses (Fig 6R',U white arrowhead, Video 8). In contrast, *Scx-GFP* prepatterning in muscle connective tissues was preserved in *Myf5*$^{nlacZ/nlacZ}$ mutants and *Scx-GFP*+ condensations formed at the positions of prospective (although absent) recti muscles (Fig 6S,S',V, white arrowheads). This situation is similar to the presence of individual tendons on the distal autopod of muscle-less limbs (Huang et al., 2015; Kardon, 1998) and branchial arches (Grenier et al., 2009). However, at later stages, tendons did not continue their maturation in the absence of EOMs (Suppl Fig

6Q-R', video 9 and 10), reinforcing the notion that, as in most other anatomical locations (Huang, 2017), tendon differentiation and maintenance appear to ultimately rely on muscle-tendon interactions. In summary, ATRA produced by the developping eye influences the organization of the entire neural crest derived POM, including tendon condensations and EOM insertions in the POM-ring. Moreover, given that retinoic acid signaling exerts this action with a time interval that precedes and overlaps with that of EOM anlage segregation into individual muscle masses, we propose that EOM and insertion site patterning are regulated in a coordinated manner.

DISCUSSION

The stark differences in embryological origins, function and susceptibility to disease among cranial and somite-derived muscles (Sambasivan et al., 2011), provides impetus to study in detail the morphogenesis of different muscle groups and their integration as part of the musculoskeletal system. Here we focused on EOMs, an evolutionarly conserved group of muscles that are precisely engineered for fine displacement of the eyeball, and thus crucial for visual acuity. Using genetic and 3D imaging approaches, we analysed EOM development from their emergence as a unique anlage to the establishment of a fully formed functional unit with insertions in the sclera, which sets it apart from classical muscle-to-bone insertions studied to date. We identified a spatiotemporal window in which retinoic acid signaling from the target organ is required for patterning of NCC-derived soft tissues of the POM. These findings provide insights into the deployment of site-specific programs for the establishment of anatomically distinct muscle functional units, with precise definition of muscle shapes and topographical wiring of their tendon attachments.

Dual origin of EOM insertions

The connective tissues of the rostral cranium (bone, cartilage, tendon and muscle connective tissue) were reported to be derived from the neural crest (Nassari et al., 2017; Noden and Francis-West, 2006; Ziermann et al., 2018). However, the hypochiasmatic cartilages, from which the recti muscles originate in mammals, are an exception to this rule as they are mesoderm-derived (McBratney-Owen et al., 2008). Here, we found that at this location, tendon and muscle connective tissue are also of mesodermal origin. As such, EOM originate in mesoderm-derived bone and insert in NCC-derived fibrous tissue of the sclera with muscle connective tissue following the embryonic origins of the respective attachments as observed in other anatomical locations (Heude et al., 2018). Taken together, our observations redefine a novel boundary for NCC contribution to the connective tissues of the

458 periocular region and suggest that at their origin, the EOMs and their associated connective
459 tissues might have evolved neomorphically *in situ* from the same mesodermal source.
460
461 **RA responsiveness on the POM**
462 Previous studies showed that NCC have a critical role in the acquisition of cranial
463 muscle morphology (Bohnsack et al., 2011; McGurk et al., 2017; Shimizu et al., 2018; Tokita
464 and Schneider, 2009; von Scheven et al., 2006). Our data using the *Rare*^{CreERT2} reporter and
465 following invalidation of *Rarb/Rarg* in NCC derivatives suggest that the action of retinoic acid
466 signaling on EOM patterning is also indirect, through its action on periocular connective
467 tissues.
468 The observation that BMS493 treatments to impair ATRA signaling results in a more
469 severe phenotype than that observed in *Aldh1a3* mutants could have several explanations.
470 First, BMS493 is not a RAR antagonist but pan-RAR inverse agonist, which is capable of
471 repressing RAR basal activity by favoring the recruitment of corepressors and promoting
472 chromatin compaction (Germain et al., 2009). Second, additional sources of ATRA could
473 signal to the POM and be inhibited by the BMS493 treatment. Candidates include *Aldh1a1*
474 (retina), *Aldh1a2* (temporal mesenchyme) and *Cyp1B1*, a member of the cytochrome p450
475 family of mono-oxygenases which can generate ATRA in the retina in a retinaldehyde
476 dehydrogenease-independent manner (Chambers et al., 2007). Noneless, the severe
477 patterning phenotypes observed in the *Aldh1a3* single mutant suggest that the local
478 synthesis of ATRA in the RPE, optic stalk and ventral retina at early stages (≈E10.5) cannot
479 be fully compensated by the action of other retinaldehyde dehydrogeneases in adjacent
480 tissues (this study, (Dupe et al., 2003; Harding and Moosajee, 2019)). Interestingly, the
481 constitutive *RARE-hsp68-lacZ* transgene displays strong reporter activity in the retina and
482 RPE (Matt et al., 2005; Rossant et al., 1991). Thus, we cannot exclude the possibility that
483 some of the phenotypes observed in periocular connective tissues of the *Aldh1a3* mutant are
484 partly due to changes in signalling pathways downstream of ATRA in the retina and/or RPE,
485 that subsequently act in the POM.
486
487 **EOM and tendon patterning are concerted processes under RA control**
488 We identified a short temporal window (E10.5-E11.75) where ATRA is essential for the
489 precise morphogenesis of several elements of the POM, including the formation of tendon
490 condensations and insertion sites in the POM-ring. These phenotypes are already evident
491 from E11.75, a stage where the EOM still figures as a muscle anlage. Interestingly, analysis
492 of chick and mouse limb development also identified a short time window where limb
493 mesenchyme perturbations result later in muscle and tendon patterning defects (Chevallier
494 and Kieny, 1982; Hasson et al., 2010). Moreover, concomitant muscle and tendon defects

have been observed in the chick limb and zebrafish jaw upon retinoic acid signaling misregulation (McGurk et al., 2017; Rodriguez-Guzman et al., 2007). Altogether, these results suggest that at certain anatomical locations including the EOMs, endogenous local variations in the concentration of retinoids contribute to the establishment of *Scx-GFP+* condensations, a critical step in muscle functional unit assembly. As ectopic muscles masses are associated with ectopic tendons upon ATRA deficiency, one possible explanation is that retinoic acid signaling directly controls *Scx-GFP+* condensations, which in turn help organize the adjacent forming muscles. On the other hand, it is also possible that connective tissue mispatterning upon ATRA deficiency determines the organization of the muscle masses and the muscle tips direct the organization of the *Scx-GFP+* condensations.

Role of RA in the integration of EOM patterning and insertion site formation

The EOMs insert into the sclera, a non-bone structure in mammals. The generation of 4 attachment points that precisely mirror the position of the 4 recti muscles is a morphogenesis conundrum, as details on their specification are scarse. Four mesenchymal condensations have been described at the periphery of the developing optic cup in cat and human embryos, in positions facing the locations of the recti muscles (Gilbert, 1957; Gilbert, 1947). In the mouse, at equivalent developmental timepoints (E11.5-E12.5) and homologous positions, apoptotic foci were observed and suggested to provide attachment for the recti muscles (Sulik et al., 2001). Using 3D-imaging, we showed that at E11.75, the apoptotic foci are aligned with *Scx-GFP+* condensations that project medially, before any sign of splitting of the EOM anlage. As the apoptotic foci decrease in size from E12.5 onwards concomittant with ongoing muscle splitting and tendon formation, it is possible that they initially presage the POM for future tendon insertions, but are not required for attachment *per se*. These foci appear in a SOX9+ PITX2+ domain of the future sclera, however, to our knowledge their presence has not been reported in superstructures at other anatomical locations.

In agreement with the role of RA in the induction of cell death in another locations in the embryo (Dupe et al., 2003), our study shows that upon perturbation of RA signaling, the apoptotic foci in the POM are absent or severely reduced. However, it is also possible that the loss of foci upon RA inhibition is secondary to loss or mispatterning of the SOX9+ PITX2+ POM-ring. Thus, it will be of interest to determine if null or NCC specific mutations in PITX2 affect the patterns or amount of naturally occurring cell death in the periocular condensations. Although our work sheds light on the genetic mechanisms that regulate EOM insertion, the cellular mechanisms underlying this process remains undefined. It is tempting to speculate that the apoptotic foci are related to the disappearance of signaling centers (Jernvall et al., 1998; Nonomura et al., 2013) or compaction-mediated cell death and

extrusion (Moreno et al., 2019). Future experiments directed towards modifying the amount or timing of cell death will be informative.

Few reports have demonstrated that mispatterning of specific muscles is coupled with aberrant superstructures (Colasanto et al., 2016; Swinehart et al., 2013; Tokita and Schneider, 2009) or removal of the prospective tendon attachment sites (Rodriguez-Guzman et al., 2007). Our results, are in agreement with that model given that EOM mispatterning is concomitant with aberrant EOM insertions. Given that mammals do not develop a cartilage layer within the sclera (Franz-Odendaal and Vickaryous, 2006; Thompson et al., 2010), expression of SOX9 in the POM-ring of mouse embryos at the time of EOM patterning is intriguing. SOX9 expression at this level appears to be dependent on a functional RPE and ATRA ((Thompson et al., 2010), this study). In this context, our data suggest that transient SOX9 expression may represent a redeployment of the developmental module for tendon attachment, despite the fact there is no cartilage in the mammalian sclera. Finally, transcriptome analysis revealed the existence of global and regional regulatory modules for superstructure patterning in the limb bones (Eyal et al., 2019), offering a mechanism to induce variations in attachment sites without having to rewrite the entire skeletogenic program (Eyal et al., 2019). As several markers of the POM (*Pitx2*, *Foxc1/2*) and retinoic acid signaling modulators (*Cyp26a1/b1*) were identified as part of specific limb superstructure signatures (Eyal et al., 2019), it is tempting to speculate that those genes also play a conserved role in the generation of the attachment module of the EOMs.

Conclusion

The developing eye has been proposed to be key organizer of craniofacial development, independent of its role in vision (Kish et al., 2011). This notion is based on the role of the eye for proper NCC migration to the periocular region (Langenberg et al., 2008), the common association of ocular and craniofacial developmental abnormalities (Zein, 2012) and the initial development of an eye in blind vertebrate species (Durand, 1976; Kish et al., 2011; Yamamoto et al., 2004). Moreover, as the appearence of a "camera-type" eye is a vertebrate innovation (Lamb et al., 2007) and the EOM are already present in lamprey (Suzuki et al., 2016), it is possible that muscles and their target tissue might have co-evolved. Here, by characterizing coordinated patterning of the EOMs, their respective tendons and attachments, our findings illustrate further the role of the developing eye as a signaling center allowing integration of the EOM functional unit in the POM. Our results show that the tissue interactions during the development of this craniofacial muscle unit share features with those described in the limb, but with additional regional properties (e.g. cell death, specification of attachments in the sclera) that seem to have been specifically incorporated into this group. Moreover, the capacity to instruct muscle patterning through variations in connective tissue

derivatives, provides a mechanism to explain the plasticity of the musculoskeletal system at the anatomical and inter-species levels, while ensuring structural and functional integration during evolution. These findings also imply that the generation of musculoskeletal units do not require major restructuring of the developmental programs of all the tissues implicated. Instead, co-option of a general program and simultaneous addition of local features appear to elaborate musculoskeletal diversity.

Figure Legends

Fig1. Lineage contributions to the EOM functional unit.

(A-H) Neural Crest cell (NCC, *Wnt1*^{Cre};*R26*^{Tom}) and mesoderm (*Mesp1*^{Cre};*R26*^{Tom}) lineage contributions to the periocular region on coronal cryosections of E13.5 embryos, combined with immunostaining for GFP (*Tg:Scx-GFP* tendon reporter), muscle (PAX7/MYOD/MYOG, myogenic markers), SOX9 (chondrogenic/scleral marker) and PITX2 (EOM muscle progenitor and periocular mesenchyme marker). Sections at ventral (A-D) and dorsal (E-H) levels. Asterisks in 1A-D denote tendon insertion sites. Dashed regions in A-H delimitate the periocular mesenchyme. Panels A-B and E-F, an anti-DsRed antibody was used to enhance the R26^{Tom} signal. Panels C-D and G-H, the endogenous reporter signal was used. C,D and G,H are consecutive sections to the ones shown in panels A,B and E,F respectively. (n=3 per condition).

az, annulus of zinn; ce, corneal ectoderm; eom, extraocular muscles; le, lens; l-pom, lateral periocular mesenchyme, at the level of the tendon insertions; mct, muscle connective tissue; m-pom, medial periocular mesenchyme; r, retina; rpe, retinal pigmented epithelium; s, sclera; t, tendon (at the level of the insertion); ti, tendon insertion site.

Fig2. Developmental timing of EOM functional unit components

(A-C) WMIF for the MYOD/MYOG/Desmin (myogenic differentiation markers) (A, B) and MF20 (myofibers) (C) at the indicated embryonic stages. Medial views (left eye).

(D) WMIF for MYOD/Desmin (labeling the EOM anlage, shown as isosurface for clarity) and PITX2 (labelling the POM and EOM anlage) on E11.75 embryos (left eye). Lateral and medial views as schemes.

(E) Whole Mount LysotrackerRed staining of the periocular region at the indicated stages. The POM is delimited with a dotted line. Anterior (a), posterior (p), medial (m) and lateral (l) apototic foci are indicated. Asterisks indicate apoptotic foci with reduced intensity from E12.5 onwards.

603 **(F-I)** Immunostaining of lateral POM in coronal sections of E12 *Wnt1^{Cre};R26^{Tom};Scx-GFP*
604 embryos. Images correspond to insertion site of superior rectus muscle in POM. G,
605 immunostaining of section adjacent to the one shown in (F,H,I; channels split for clarity).
606 **(J,J')** Tunel, LysotrackerRed and SOX9 staining of area depicted in I. Scale bars 50 microns.
607 **(K,N)** Immunostaining of lateral POM in coronal sections of E13.5 *Wnt1^{Cre};R26^{Tom};Scx-GFP*
608 embryos. Images correspond to insertion site of superior rectus muscle in POM. L,
609 immunostaining of section adjacent to the one shown in (K,M,N; channels split for clarity).
610 **(O-S)** Immunostaining on coronal sections of E14.5 *Scx-GFP* embryos. Tnc (Tenascin), GFP
611 and PITX2 co-localize in tendons at level of insertion. MF20 (O-Q) and Smooth muscle actin
612 (SMA) (R,S) were used to label EOM muscle. Dashes in R,S were drawn according to GFP
613 labelling on adjacent sections. Asterisks in O denote tendon insertion sites. Low
614 magnification views of panels P-S are shown in Suppl Fig 2. (n=3 per condition).
615 anl, anlage; apop, apoptosis spots; eom, extraocular muscles; ir, inferior rectus; le, lens; lg,
616 lacrimal gland sulcus; t, tendon (at the level of the insertion); lr, lateral rectus; i, inferior EOM
617 anlage projection; io, inferior oblique; mr, medial rectus; pom-r, periocular mesenchyme ring;
618 m-pom, medial periocular mesenchyme; rpe, retinal pigmented epithelium; s, sclera; s,
619 superior EOM anlage projection; sr, superior rectus; so, superior oblique; rb, retractor bulbi.
620
621 **Fig3. EOM morphogenesis in mutants with eye defects**
622 **(A-C)** μCT-based 3D reconstruction of EOM, eyeball, optic nerve and lens in E13.5 control
623 (A), *Pax6$^{Sey/+}$* (B) and *Pax6$^{Sey/Sey}$* embryos (C). Note that in heterozygote embryos EOM
624 patterning proceeds normally despite having a smaller retina and lens (n=3).
625
626 **Fig4. Extraocular muscle morphogenesis is dependent on ATRA**
627 **(A)** Immunostaining for ALDH1A3 on coronal sections of E10.5, E11.5 and E12.5 control
628 embryos (n=2).
629 **(B)** Scheme of retinoic acid signaling pathway with key enzymes for oxidation of retinol and
630 retinaldehyde (pink) and mutants/inhibitors used in this study (blue).
631 **(C-D''')** μCT-based 3D-reconstruction of chondrogenic mesenchymal condensations of nasal
632 capsule, trabecular cartilage, EOM, eyeball, optic nerve and lens in E13.5 control, *Aldh1a3^{KO}*
633 and BMS treated embryos. EOM visualization in context of whole head (D), nasal capsule
634 (D'-D''), trabecular capsule (D''').
635 **(E)** Raw μCT data of panels in C-D (n=2)
636 **(F-H)** EOM 3D-reconstructions of whole mount MyHC immunostaining of E13.5 control (F),
637 *Aldh1a3^{KO}* (G) and BMS treated embryos (H) (n>9). (1-7) denote non-segregated muscle
638 masses with differential fiber orientation (see also Suppl Fig 5E). Raw immunostaining data
639 for MyHC (muscle) and Tenascin (Tnc, tendon) are shown in panels F'-H'.

640 **(I)** Relative EOM volume (compared to control) of E13.5 3D-reconstructed whole mount
641 immunostained EOM of E13.5 control, *Aldh1a3*^{KO} and BMS treated embryos. Each dot
642 represents an individual embryo (n>9).
643 dr, dorsal retina; hc, hypochiasmatic cartilage; io, inferior oblique; ir, inferior rectus; le, lens;
644 lr, lateral rectus; mr, medial rectus; os, optic stalk; se, surface ectoderm; so, superior oblique;
645 sr, superior rectus; rb, retractor bulbi; rpe, retinal pigmented epithelium; vr, ventral retina
646
647 **Fig5. Periocular connective tissues are responsive to retinoic acid signaling**
648 **(A)** Scheme of mouse alleles used. *Tg:RARE*^{CreERT2} line is composed of three RARE
649 elements from the *Rarb* gene fused to hsp68 promoter driving expression of a tamoxifen-
650 inducible *Cre*^{ERT2} recombinase. Crossing this line with the *R26*^{mTmG} reporter line, allows
651 permanent labelling of the ATRA-responsive cells and tracing of their descendents.
652 **(B)** Strategy used to determine cell-types reponsive to retinoic acid signaling in
653 *Tg:RARE*^{CreERT2}*::R26*^{mTmG} embryos. Tamoxifen was injected to pregnant females at E9.75 or
654 E10.5 and cells of the periocular region isolated at E11.75 or E12.5.
655 **(C)** Percentage of recombined (GFP+) cells in connective tissue (CT) and myogenic (Myog)
656 populations for different treatments. Each dot represents an individual embryo (n>4
657 embryos/condition).
658 **(D-G')** Whole mount immunostaining for SMA (smooth muscle actin, differentiated muscle),
659 GFP (ATRA-responsive cells) and SOX9 (periocular mesenchyme) at indicated embryonic
660 stages. (D-E') 3D-reconstructed EOM labelling. Arrowhead indicates an increased number of
661 reporter positive cells surrounding the optic nerve (asterisk) at E12. (F-G') Segmented
662 periocular region. pom-ring (dotted lines) (n=3).
663 **(H-H')** Coronal sections at different eye levels of E11.75 *Tg:RARE*^{CreERT2}*::R26*^{mTmG} embryos
664 immunostained for GFP (RA-responsive cells) and MYOD/MYOG (muscle). Higher
665 magnification views as insets. Arrowheads mark presence of RA-responsive cells in medial
666 periocular mesenchyme (H) and lateral-POM (H'). Asterisks indicate sporadic labelling in
667 myogenic cells (n=3).
668 **(I-J')** EOM 3D-reconstructions of whole mount MF20 immunostaining of E12.5 of control
669 (*Wnt1Cre: Rarb*$^{fl/+}$*:Rarg*$^{fl/+}$) (I,I') and mutant (*Wnt1*^{Cre}*:Rarb*$^{fl/fl}$*:Rarg*$^{fl/fl}$) (J,J') embryos. Medial
670 and lateral views are shown. Note absence of splitting in mutant EOM. Arrowheads indicate
671 split EOM in controls (n=2 per genotype).
672
673 **Fig 6. EOM insertions in the POM altered upon ATRA-deficiency**
674 **(A-C')** Immunostaining for Collagen XII (ColXII) on E12 coronal sections. Reduced ColXII
675 expression domain in *Aldh1a3*^{KO} (B,B') and BMS493 treated embryos (C,C') (arrowheads).

676 ColXII expression in medial-pom (future sclera) is lost (brackets). Split ColXII channel as
677 insets in (A'-C').
678 **(D-G)** Immunostaining for PITX2 (muscle progenitors, periocular mesenchyme) and
679 MYOD/MYOG (myogenic cells) on coronal E12 sections. Asterisks indicate superior oblique
680 muscle (SO). Dashed line mark periocular mesenchyme (pom). Brackets on *Aldh1a3*^{KO} and
681 BMS493 embryos indicate absence of PITX2 expression in medial-pom. Split PITX2 channel
682 as insets in (D'-G').
683 **(H-P)** Lateral views of periocular region of whole mount immunostaining (GFP, SOX9,
684 PITX2) and Lysotracker Red Staining (Lyso, apoptosis) of E12 control (H-J), *Aldh1a3*^{KO} (K-
685 M) and BMS493 treated (N-P) embryos (left eyes). *Aldh1a3*^{KO} and BMS493 embryos do not
686 show a complete pom-ring as controls (dotted lines in I). Arrowheads mark remaining
687 expression of SOX9/PITX2 in the POM of *Aldh1a3*^{KO} (L) or inhibitor treated (O) embryos.
688 Asterisks in (J,M,P) mark apoptosis spots in POM.
689 **(Q-V)** WMIF for MF20 (myofibers) and GFP (*Tg:Scx-GFP*) on control (Q,Q',T), BMS493
690 treated (R,R',U) and *Myf5*$^{nlacZ/nlacZ}$ E12 embryos (S,S',V) (left eyes). **(Q-S)** The periocular area
691 was segmented from adjacent structures for ease on visualization (dashed lines). **(T-V)**
692 Single Z-section of the segmented volume. (n=3 per condition)
693 White arrowheads in Q',S', T,V indicate correct position of tendon condensations for recti
694 muscles. Blue arrowhead in R' mark a diffuse *Scx-GFP*+ pattern at the position of the
695 mispatterned MR (medial recti) muscle and white arrowheads in R', U mark an ectopic *Scx-*
696 *GFP* condensation at the muscle tip.
697 le, lens; nlg, nasolacrimal gland; eom, extraocular muscles
698
699
700
701 **Supplementary Figure Legends**
702 **Supplementary Fig 1. Lineage contributions to the EOM functional unit.**
703 **(A-F)** Neural Crest cell (NCC, *Wnt1*^{Cre}*;R26*^{Tom}) and mesoderm (*Mesp1*^{Cre}*;R26*^{Tom}) lineage
704 contributions to the periocular region on coronal cryosections of E17.5 embryos, combined
705 with immunostaining for GFP (*Tg:Scx-GFP* tendon reporter) and muscle (Tnnt3). Sections at
706 ventral (A-F) and dorsal (A'-F') levels. Note that lateral tendons at the level of the orbit are
707 NCC-derived (A-C), whereas tendons at the levels of the annulus of zinn (D'-F') are
708 mesoderm-derived.
709 az, annulus of zinn; eom, extraocular muscles; hc, hypochiasmatic cartilage; lt, lateral tendon
710 (at the level of the insertion); mct, muscle connective tissue
711
712

713 **Supplementary Fig 2. Developmental timing of EOM functional unit components**
714 **(A-L)** Immunostaining for the indicated markers on coronal sections of E14.5 *Tg:Scx-GFP*
715 embryos. Tnc (tenascin) (n=2 per condition).
716 eom, extraocular muscles; lt, lateral tendon (at the level of the insertion; asteriks); m-pom,
717 medial periocular mesenchyme; mct, muscle connective tissue; on, optic nerve; rpe, retinal
718 pigmented epithelium
719
720 **Supplementary Fig 3. EOM morphogenesis in mutants with eye defects**
721 **(A-B)** μCT-based 3D-reconstruction of EOM and eyeball in E18.5 control (A) and
722 *Lhx2Cre:Lhx2fl/fl* (B) embryos. Arrowheads highlight some extent of EOM segregation in the
723 mutant. (A'-B') Coronal sections of control (A') and mutant (B') embryos stained with MyHC.
724 Arrowheads indicate individual EOM masses (n=2).
725 **(C-C'')** Analysis of EOM patterning in E15.5 embryos containing inversions of *Shh* genomic
726 regulatory regions (Inv(6-C2)). (C) Skeletal preparation of mutant embryos displaying
727 cyclopia. (C'-C'') μCT-based 3D reconstruction of EOM and eyeball of mutant embryos (n=2).
728
729 **Supplementary Fig 4. EOM morphogenesis is dependent retinoic acid signaling**
730 **(A)** Whole mount in situ hybridization for *Aldh1a1*, *Aldh1a2* and *Aldh1a3* in E10.5, E11.5 and
731 E12.5 embryos (n=3).
732 **(A')** In situ hybridization for *Aldh1a2* and immunostaining for ALDH1A2 and muscle (MF20)
733 on E12.5 coronal sections. ALDH1A2 is expressed in the temporal mesenchyme and muscle
734 connective tissue (n=3).
735 **(B)** μCT-based 3D-reconstruction of eyeball, optic nerve and lens of E13.5 control,
736 *Aldh1a3*^{KO} and BMS treated embryos (n=2 each genotype). The lower row is a scheme of a
737 sphere fitting the eyeball and lens, and a cylinder for the optic nerve. Note ventralization of
738 the eyeball in *Aldh1a3*^{KO} and BMS treated embryos.
739 **(C)** μCT-based 3D-reconstruction of the mesenchymal condensations of the nasal capsule
740 and trabecular cartilage of E13.5 control (white), *Aldh1a3*^{KO} (yellow) and BMS-treated
741 (green) embryos.
742 **(D-D')** EOM 3D-reconstructions of whole mount MyHC immunostaining of E13.5 of BMS-
743 treated embryos as described in Table S1. The most severe phenotype obtained in each
744 condition is shown. Two different examples of the phenotype observed upon treatment VI
745 (a,b) are shown (most and least severe). An *Aldh1a3*^{KO} embryo is shown as comparison.
746 Asterisk denote ectopic duplicated SO (superior oblique) muscle. (D') Higher magnification
747 views from D with examples of adjacent, non-split muscle masses (1,2) depicted by
748 differential fiber orientation.

749 **(E-F)** Whole mount MyHC immunostaining of E13.5 control (G) and *Rdh10*^{KO} (H) embryos.
750 Note total absence of muscle splitting in mutant (n=3 per condition).
751 ce, corneal ectoderm; dr, dorsal retina; io, inferior oblique; ir, inferior rectus; le, lens; lgb,
752 lacrimal gland bud; lr, lateral rectus; mr, medial rectus; nlg, nasolacrimal groove; np, nasal
753 pit; os, optic stalk; se, surface ectoderm; so, superior oblique; sr, superior rectus; rb, retractor
754 bulbi; rpe, retinal pigmented epithelium; tm, temporal mesenchyme; vr, ventral retina
755
756 **Supplementary Fig 5. Retinoic acid signaling responsiveness in the periocular region**
757 **(A-C)** Macroscopic views of endogenous GFP fluorescence of *Tg:RARE*^{CreERT2}*:R*^{26mTmG}
758 embryos. Tamoxifen (Tam) was injected into pregnant females at indicated time points.
759 Arroheads indicate labelling in periocular mesenchyme (POM) (n>3 per condition).
760 **(D)** Strategy used to determine responsiveness of *Tg:RARE*^{CreERT2} reporter in presence of RA
761 signaling reverse agonist BMS493. BMS493 was injected to pregnant females between E10
762 and E11.75.
763 **(E-H)** Whole mount immunostaining for MyHC (muscle), GFP (ATRA-responsive cells) of
764 control (E, F) and BMS493-treated embryos (G, H). (E, G) Medial views of 3D-reconstructed
765 EOM labelling. BMS493 treatment before and after tamoxifen induction reveals a drastic
766 decrease in GFP+ cells in the periocular region (H) compared to controls (F). Asterisks mark
767 the location of the optic nerve (n=2).
768
769 **Supplementary Fig 6. EOM insertions in the POM are altered upon ATRA-deficiency**
770 **(A-D)** Immunostaining for GFP (tendon progenitors), SOX9 (periocular mesenchyme, POM),
771 MF20 (myofibers) together with Lysotracker Red staining (Lyso, apoptosis) on coronal E12
772 sections of *Tg:Scx-GFP* control (A-B') and BMS493 treated (C-D') embryos. (B',D') higher
773 magnification views of the periocular mesenchyme (POM) region. In BMS493-treated
774 embryos, Lysotracker Red and SOX9 staining are absent in POM (D', asterisk) and SOX9
775 staining also missing in the RPE (D', double asterisk).
776 **(E-P)** Whole mount immunostaining for SOX9 and PITX2, SMA and Lysotracker Red
777 Staining of E11.75 control (E, F, N), *Aldh1a3*^{KO} (G,H, O) and BMS493-treated (I, J, P)
778 embryos (right eyes). In lateral views, neither *Aldh1a3*^{KO} or BMS493 embryos show a
779 PITX2+ pom-ring as the controls (F). Arrowheads in (G,H,J) mark remaining expression of
780 SOX9/PITX2 in POM of mutant or inhibitor treated embryos. Asterisks in (F,H,J) mark
781 apoptosis spots in POM.
782 **(N-P)** Segmented medial views of periocular region of control embryos. Volumes were
783 truncated in Z for clarity. Full view as schemes below. The PITX2+ pom-ring is continuous
784 with the medial-pom (white arrowhead, N). In mutant and inhibitor treated embryos, residual
785 PITX2 expression in POM is discontinous with the medial-POM.

786 **(Q-R)** Whole mount immunostaining for GFP and β-gal (*Myf5*^{nlacZ} reporter, myogenic
787 progenitors) of E14.5 *Tg:Scx-GFP*::*Myf5*$^{nlacZ/+}$ (Q, control) and *Tg:Scx-GFP*::*My5*$^{nlacZ/nlacZ}$ (R,
788 mutant) embryos (left eyes). Asterisk indicate few remaining β-gal+ cells in mutant. (Q',R')
789 split GFP channel. Arrowheads in R indicate the correct position of tendon condensations for
790 the 4 recti muscles although these are absent in the mutant. Lower panel, higher
791 magnification views.
792 m, extraocular muscle; anl, anlage; apop, apoptosis; m-pom, medial periocular mesenchyme;
793 l-pom, lateral periocular mesenchyme; rpe, retinal pigmented epithelium.
794
795
796 **Tables**
797 **Table 1. BMS493 injection regimes.** The same BMS493 concentration (Conc BMS) was
798 used across injection regimes, from I to VI. Pink cases mark injection time points in the
799 morning (mo), midday (mid) or evening (eve) between E10.5 and E12.5. The number of
800 embryos with different muscle phenotype severity at E13.5 are shown: (no), no altered
801 phenotype; mild (+), muscle mispatterning but overall organization retained; strong (++),
802 strong mispatterning but with a minumum of 2 muscles split; severe (+++), no or almost
803 absent splitting. n is the total number of embryos analyzed for a certain treatment type (n=38
804 embryos analyzed in total); N exp, number of times experiment was repeated.
805 **Table 2. Antibodies and resources used in this study.**
806
807 **Videos**
808 **Video 1. Temporal sequence of EOM patterning.** 3D-recontruction of whole mount
809 immunostaining of the developing EOM in embryos ranging from E11.5 to E14.5. EOM were
810 segmented from adjacent head structures and 3D-reconstructed in Imaris.
811 **Video 2.** 3D-recontruction of EOM functional unit at E11.75. Immunostaining for Muscle
812 (MF20, Cyan) and tendon (*Tg:Scx-GFP*, Green). Apoptotic foci are visualised by Lysotracker
813 Red. A clipping plane is added for clarity of visualisation. Note how tendon condensations
814 start to organize radially and towards the apoptotic foci in the POM.
815 **Video 3.** 3D-recontruction of EOM functional unit at E12.5. Immunostaining for Muscle
816 (MF20, Cyan) and tendon (*Tg:Scx-GFP*, Green). Apoptotic foci are visualised by Lysotracker
817 Red. A clipping plane is added for clarity of visualisation. Note how tendon condensations of
818 the recti muscles are more refined at this stage and project towards the apoptotic foci in the
819 POM.
820 **Video 4.** 3D-recontruction of te EOM functional unit at E13.5 of a BMS treated embryo
821 (E10.5→ E11.75). Immunostaining for Muscle (MyHC, Red) and tendon (*Tg:Scx-GFP*,

822 Green). Note the presence of tendon condensations at the tips of mispatterned muscle
823 masses.
824 **Video 5.** 3D-recontruction of whole mount immunostaining of control EOM (MyHC, Red) and
825 *Tg:Rare*^{CreERT2}*:R26*^{mTmG} reporter (GFP, Green) at E13.5 (Tamoxifen induction at E10.5).
826 EOMs are shown as isosurface for clarity of visualisation.
827 **Video 6.** 3D-recontruction of whole mount immunostaining of EOMs (MyHC, Red) and
828 *Tg:Rare*^{CreERT2}*:R26*^{mTmG} reporter (GFP, Green) at E13.5 (Tamoxifen induction at E10.5) on
829 BMS-treated embryos (E10.5 → E11.75). EOMs are shown as isosurface for clarity of
830 visualisation.
831 **Video 7.** 3D-recontruction of whole mount immunostaining of control EOM (MyHC, Red) and
832 tendon (*Tg:Scx-GFP*, Green) at E12.5. A clipping plane has been added for clarity of
833 visualisation.
834 **Video 8.** 3D-recontruction of whole mount immunostaining of EOM (MyHC, Red) and
835 tendons (*Tg:Scx-GFP*, Green) of a BMS-treated embryo (E10.5 → E11.75) at E12.5. A
836 clipping plane has been added for clarity of visualisation. Note that distribution of Scx+ cells
837 is more difuse than for controls (Video 7), but an *Scx-GFP*+ condensation is present at the
838 tip of the inferior muscle mass.
839 **Video 9.** 3D-recontruction of whole mount immunostaining of control EOM (MYOG/MYOG,
840 Red) and tendon (*Tg:Scx-GFP*, Green) at E14.5.
841 **Video 10.** 3D-recontruction of whole mount immunostaining of *Myf5*$^{nlacZ/nlacZ}$ EOM
842 (MYOG/MYOG, Red) and tendon (*Tg:Scx-GFP*, Green) at E14.5.
843
844
845 **Materials and methods**
846 **Mouse strains and animal information**
847 Animals were handled as per European Community guidelines and the ethics committee of
848 the Institut Pasteur (CETEA) approved protocols. The following strains were previously
849 described: *Mesp1*^{Cre} (Saga et al., 1999), *Tg:Wnt1*^{Cre} (Danielian et al., 1998), *Tg:Rare*^{CreERT2}
850 (Schedl et al., unpublished), *R26*^{Tom} (Ai9; (Madisen et al., 2010)), *R26*^{mTmG} (Muzumdar et al.,
851 2007), *Tg:Scx-GFP* (Pryce et al., 2007), *Myf5*^{nlacZ} (Tajbakhsh et al., 1996), *Aldh1a3*^{KO} (Dupe
852 et al., 2003), *Rarb*^{flox} (Chapellier et al., 2002a), *Rarg*^{flox}, (Chapellier et al., 2002b), *Rdh10*^{KO}
853 (Rhinn et al., 2011), *Pax6*$^{Sey/Sey}$ (Roberts, 1967). *Rdh10*^{KO} embryos were received from the
854 laboratory of Pascal Dollé. *Wnt1Cre:Rarb*$^{fl/fl}$*:Rarg*$^{fl/fl}$ embryos were received from the
855 laboratory of Valerie Dupé. *Pax6*$^{Sey/Sey}$ and control embryos were received from the
856 laboratory of James Briscoe. *Lhx2*^{Cre}*;Lhx2*$^{fl/fl}$ (Hagglund et al., 2011) were received from the
857 laboratory of Leif Carlsson. *Shh(invC-6)2* embryos were received from the laboratory of
858 François Spitz.

859 To generate experimental embryos for *Mesp1*^{Cre} or *Wnt1*^{Cre} together with *Tg:Scx-GFP* and
860 *R26*^{Tom} lineage tracings, Cre/+ males were crossed with *Tg:Scx-GFP::R26*$^{Tom/Tom}$ females.
861 Mice were kept on a mixed genetic background C57BL/6JRj and DBA/2JRj (B6D2F1, Janvier
862 Labs). Mouse embryos and foetuses were collected between embryonic day (E) E10 and
863 E18.5, with noon on the day of the vaginal plug considered as E0.5. Pregnant females were
864 euthanised by cervical dislocation.
865 To induce recombination with the *Rare*^{CreERT2}*:R26*^{mTmG} line, 5mg of tamoxifen (Sigma
866 #T5648) were administered by gavage to pregnant females. A 25mg/ml stock solution in 5%
867 ethanol and 95% sunflower seed oil was prepared by thorough resuspention with rocking at
868 4°C.
869 To inhibit retinoic acid signaling, pregnant females of relevant genotypes were injected
870 intraperitoneally with 10mg/kg of BMS493 (Tocris, 3509), a pan-retinoic acid receptor (pan-
871 RAR) inverse agonist. A 5mg/ml BMS493 stock solution in DMSO (SIGMA, D2650) was
872 prepared and stored in single use aliquots at -20°C in tight cap tubes. At the time of injection,
873 the aliquot was thawed, 200ul of sterile PBS was added per 50ul aliquot and injected
874 immediately.
875
876 **Immunofluorescence**
877 Embryos were fixed 2.5h in 4% paraformaldhehyde (PFA; 15710, Electron Microscopy
878 Sciences) in PBS with 0,2-0,5% Triton X-100 (according to the embryonic stage) at 4°C and
879 washed overnight at 4°C in PBS. For cryosectioning, embryos were equilibrated in 30%
880 sucrose in PBS overnight at 4°C and embedded in OCT. Cryosections (16-18µm) were
881 allowed to dry at RT for 30 min and washed in PBS. Immunostaining was performed as
882 described in (Comai et al., 2019). TUNEL staining, that marks double strand breaks, was
883 performed with the In Situ Cell Death Detection Kit/Fluorescein (Roche, 11 684 795 910).
884 Slides were first pretreated with a 2:1 mix of Ethanol:Acetic Acid 5min -20C, washed twice 20
885 min with PBS at RT and processed for TUNEL staining as described by the manufacturer.
886 For whole mount immunostaining, embryos were fixed and washed as above and dehydrated
887 in 50% Methanol in PBS and twice in 100% Methanol, 30min each at RT and kept at -20˚C
888 till needed. Heads were rehydrated, the periocular region was micro-dissected in PBS and
889 immunostaining performed as described in (Comai et al., 2019). For embryos older than
890 E13.5, the alternative pretreatment (containing 0.1%Tween-20, 0.1%TritonX100,
891 0.1%Deoxycholate, 0.1%NP40, 20%DMSO in PBS) and primary antibody immunolabelling
892 steps of the idisco protocol (https://idisco.info/idisco-protocol/) were generally used. In all
893 cases secondary antibodies were applied in blocking buffer as described in (Comai et al.,
894 2019) for >4 days at 4C with rocking. After immunolabelling, samples washed in
895 0.1%Tween/PBS, dehydrated in 50% Methanol in PBS, 100% Methanol 10min each at RT,

896 cleared with a mix benzyl alcohol and benzyl benzoate (BABB) and mounted for imaging as
897 described in (Yokomizo et al., 2012).
898 For detection of cell death in whole mount live tissues, LysoTracker Red staining was done,
899 as it reveals lysosomal activity correlated with increased cell death (Fogel et al., 2012;
900 Zucker et al., 1999). Embryos were quickly dissected in HBSS (Invitrogen, 14025-092),
901 incubated in 2ml tubes containing 5μM of LysoTracker™ Red DND-99 (Molecular Probes,
902 L7528) 45min at 37˚C with rocking in the dark, washed twice in PBS, fixed and processed for
903 cryosections or whole mount immunostaining as above.
904
905 **Antibodies**
906 Primary and secondary antibodies used in this study are listed in Table 2. To detect
907 differenting EOM we used: a-smooth muscle actin (SMA), which is transiently expressed in
908 differentiating myoblasts and myotubes (Babai et al., 1990; Li et al., 1996; Sawtell and
909 Lessard, 1989); Desmin, an early cytoskeletal muscle protein expressed in myoblasts,
910 myotubes and myofibers (Babai et al., 1990; Li et al., 1993) and myosin heavy chain (MF20)
911 to label sarcomeric myosin (Bader et al., 1982).
912
913 **Static Imaging**
914 A Zeiss SteREO Discovery V20 macroscope was used for imaging the endogenous
915 fluorescence of whole embryos at the time of dissection. For tissue sections and whole
916 mount immunostaining of cleared embryos a LSM700 and a LSM800 laser-scanning
917 confocal microscope with ZEN software (Carl Zeiss) were used.
918 All images were assembled in Adobe Photoshop and InDesign (Adobe Systems). Volume-3D
919 rendering of the z-stack series was performed in Imaris (version 7.2.1) software (Bitplane).
920 For ease of EOM visualization, the Z-stack volumes were first manually segmented to define
921 the EOM or the whole POM area using the Isosurface Imaris function. The signal outside the
922 isosurface was set to zero, the corresponding channel duplicated and subsequently a new
923 isosurface was created using automatic thresholding on the new channel.
924
925 **In Situ Hybridization**
926 Whole-mount in situ hybridization with digoxigenin-labeled antisense mRNA probes was
927 performed as described previously (Comai et al., 2014). The Aldh1a1, Aldh1a2, Aldh1a3
928 probes were previously described (Matt et al., 2005; Molotkov et al., 2006).
929
930
931 **micro-CT (micro computed tomography) analysis**

932 The tissue contrasting protocol has been adapted from the original protocol developed by
933 (Metscher, 2009) and applied to mouse embryos as described in (Kaucka et al., 2018) and
934 (Heude et al., 2018). For tissue contrasting, E13.5 embryos were stained in 0.5% PTA
935 (phospho-tungstic acid) in 90% Methanol for 4 days, E15.5 embryos were stained in 0.7%
936 PTA in 90% Methanol for 1 week.
937 The μCT analysis of the embryos was conducted using the GE phoenix v|tome|x L 240 (GE
938 Sensing and Inspection Technologies GmbH, Germany), equipped with a 180 kV/15W
939 maximum power nanofocus X-ray tube and flat panel detector DXR250 with 2048 × 2048
940 pixel, 200 × 200 μm pixel size. The exposure time of the detector was 900 ms in every
941 position over 360°. Three projections were acquired and averaged in every position for
942 reduction of the noise in μCT data. The acceleration voltage was set to 60 kV and tube
943 current to 200 μA. The radiation was filtered by 0.2 mm of aluminium plate. The voxel size of
944 obtained volumes (depending on a size of an embryo) appeared in the range of 2 μm - 6 μm.
945 The tomographic reconstructions were performed using GE phoenix datos|x 2.0 3D
946 computed tomography software (GE Sensing and Inspection Technologies GmbH,
947 Germany). The EOM, eye and cartilages in the embryo head were segmented by an operator
948 with semi-automatic tools within Avizo - 3D image data processing software (FEI, USA). The
949 3D segmented region was transformed to a polygonal mesh as a STL file, imported to VG
950 Studio MAX 2.2 software (Volume Graphics GmbH, Germany) for surface smoothing and 3D
951 visualisation.
952
953 **Cell isolation from the periocular region**
954 The periocular region of *Rare*^{CreERT2}*:R26*^{mTmG} embryos (including the eye itself) was micro-
955 dissected and minced with small scissors inside a 2ml Epperndorf tube. 1ml of TrypLE™
956 Express (Invitrogen, 12604013) was added to each tube incubated for 15min at 37°C with
957 agitation. Samples were resuspended by gently pipetting up and down 10-15 times using a
958 P1000 pipette. Upon addition of 1ml of culture media containing (10μg/ml) DNaseI (Roche,
959 11284932001) , samples were spun 15' 500g at RT, pellet resuspended in 400ul of culture
960 media containing of 20% foetal bovine serum (FBS; Gibco), 1% Penicillin-Streptomycin
961 (15140 Gibco), 2% Ultroser G (15950-017, Pall Biosepra) in 50:50 DMEM:F12 (31966 and
962 31765, Gibco) and plated on individual wells of 8 well glass bottom dishes (Ibidi, 80826)
963 coated with 1 mg/ml of Matrigel (354234, BD Biosciences). Cells were allowed to attach for
964 8h at 37 °C 5% CO_2, washed with PBS and fixed 15 min RT with 4% PFA/PBS. After fixation,
965 cells were washed in PBS and permeabilized with 0.5% Triton in PBS X-100 5 min at RT.
966 After three washes in PBS (5min each), cells were blocked with 20% goat serum in PBS 1 h
967 at RT. Primary antibodies were added to cells in 2% goat serum in PBS for 2 h at RT or ON

968 at 4C. Cells were washed three times with PBS, incubated with secondary antibodies 1 h at
969 RT, washed in PBS and kept in PBS for imaging.
970
971 **Statistics**
972 The number of embryos of each genotype used for analysis is indicated in the figure legends
973 and Table 1. The graphs were plotted and statistical analyses were performed using Prism8
974 (GraphPad Software, Inc). All data points are presented as mean ± SEM (error bars).
975 Statistical tests used for analysis are indicated on the respective figure legends. P values
976 less than 0.05 were considered significant (*p < 0.05; **p < 0.01; ***p < 0.001).
977
978 **Acknowledgements**
979 We acknowledge funding support from the Institut Pasteur, Association Française contre le
980 Myopathies, Agence Nationale de la Recherche (Laboratoire d'Excellence Revive,
981 Investissement d'Avenir; ANR-10-LABX-73) and the Centre National de la Recherche
982 Scientifique. We gratefully acknowledge the UtechS Photonic BioImaging (Imagopole),
983 C2RT, Institut Pasteur, supported by the French National Research Agency (France
984 BioImaging; ANR-10–INSB–04; Investments for the Future). MT, TZ and JK acknowledge the
985 project CEITEC 2020 (LQ1601) with financial support from the Ministry of Education, Youth
986 and Sports of the Czech Republic under the National Sustainability Programme II and Ceitec
987 Nano+ project CZ.02.01/0.0./.0.0./16_013/0001728 under the program OP RDE. MT was
988 financially supported by by the Brno City Municipality as a Brno Ph.D. Talent Scholarship
989 Holder. The funders had no role in study design, data collection and analysis, decision to
990 publish, or preparation of the manuscript.
991
992 **Competing interests**
993 The authors declare no competing interests.
994
995
996 **References**

997 Babai, F., Musevi-Aghdam, J., Schurch, W., Royal, A., and Gabbiani, G. (1990). Coexpression of
998 alpha-sarcomeric actin, alpha-smooth muscle actin and desmin during myogenesis in rat and mouse
999 embryos I. Skeletal muscle. Differentiation *44*, 132-142.

1000 Bader, D., Masaki, T., and Fischman, D.A. (1982). Immunochemical analysis of myosin heavy chain
1001 during avian myogenesis in vivo and in vitro. The Journal of cell biology *95*, 763-770.

1002 Blitz, E., Sharir, A., Akiyama, H., and Zelzer, E. (2013). Tendon-bone attachment unit is formed
1003 modularly by a distinct pool of Scx- and Sox9-positive progenitors. Development *140*, 2680-2690.

1004 Blitz, E., Viukov, S., Sharir, A., Shwartz, Y., Galloway, J.L., Pryce, B.A., Johnson, R.L., Tabin, C.J.,
1005 Schweitzer, R., and Zelzer, E. (2009). Bone ridge patterning during musculoskeletal assembly is

1006 mediated through SCX regulation of Bmp4 at the tendon-skeleton junction. Developmental cell *17*,
1007 861-873.

1008 Bohnsack, B.L., Gallina, D., Thompson, H., Kasprick, D.S., Lucarelli, M.J., Dootz, G., Nelson, C.,
1009 McGonnell, I.M., and Kahana, A. (2011). Development of extraocular muscles requires early signals
1010 from periocular neural crest and the developing eye. Archives of ophthalmology *129*, 1030-1041.

1011 Bohnsack, B.L., Kasprick, D.S., Kish, P.E., Goldman, D., and Kahana, A. (2012). A zebrafish model of
1012 axenfeld-rieger syndrome reveals that pitx2 regulation by retinoic acid is essential for ocular and
1013 craniofacial development. Investigative ophthalmology & visual science *53*, 7-22.

1014 Chambers, D., Wilson, L., Maden, M., and Lumsden, A. (2007). RALDH-independent generation of
1015 retinoic acid during vertebrate embryogenesis by CYP1B1. Development *134*, 1369-1383.

1016 Chapellier, B., Mark, M., Bastien, J., Dierich, A., LeMeur, M., Chambon, P., and Ghyselinck, N.B.
1017 (2002a). A conditional floxed (loxP-flanked) allele for the retinoic acid receptor beta (RARbeta) gene.
1018 Genesis *32*, 91-94.

1019 Chapellier, B., Mark, M., Garnier, J.M., Dierich, A., Chambon, P., and Ghyselinck, N.B. (2002b). A
1020 conditional floxed (loxP-flanked) allele for the retinoic acid receptor gamma (RARgamma) gene.
1021 Genesis *32*, 95-98.

1022 Chawla, B., Schley, E., Williams, A.L., and Bohnsack, B.L. (2016). Retinoic Acid and Pitx2 Regulate
1023 Early Neural Crest Survival and Migration in Craniofacial and Ocular Development. Birth Defects Res
1024 B Dev Reprod Toxicol *107*, 126-135.

1025 Chevallier, A., and Kieny, M. (1982). On the role of the connective tissue in the patterning of the chick
1026 limb musculature. Wilehm Roux Arch Dev Biol *191*, 277-280.

1027 Colasanto, M.P., Eyal, S., Mohassel, P., Bamshad, M., Bonnemann, C.G., Zelzer, E., Moon, A.M., and
1028 Kardon, G. (2016). Development of a subset of forelimb muscles and their attachment sites requires
1029 the ulnar-mammary syndrome gene Tbx3. Dis Model Mech *9*, 1257-1269.

1030 Comai, G., Heude, E., Mella, S., Paisant, S., Pala, F., Gallardo, M., Langa, F., Kardon, G.,
1031 Gopalakrishnan, S., and Tajbakhsh, S. (2019). A distinct cardiopharyngeal mesoderm genetic
1032 hierarchy establishes antero-posterior patterning of esophagus striated muscle. Elife *8*.

1033 Comai, G., Sambasivan, R., Gopalakrishnan, S., and Tajbakhsh, S. (2014). Variations in the efficiency
1034 of lineage marking and ablation confound distinctions between myogenic cell populations.
1035 Developmental cell *31*, 654-667.

1036 Couly, G.F., Coltey, P.M., and Douarin, N.M.L. (1992). The developmental fate of the cephalic
1037 mesoderm in quail-chick chimeras. Development *114*, 1-15.

1038 Creuzet, S., Couly, G., and Le Douarin, N.M. (2005). Patterning the neural crest derivatives during
1039 development of the vertebrate head: insights from avian studies. J Anat *207*, 447-459.

1040 Cunningham, T.J., and Duester, G. (2015). Mechanisms of retinoic acid signalling and its roles in
1041 organ and limb development. Nature reviews Molecular cell biology *16*, 110-123.

1042 Cvekl, A., and Wang, W.L. (2009). Retinoic acid signaling in mammalian eye development. Exp Eye
1043 Res *89*, 280-291.

1044 Danielian, P.S., Muccino, D., Rowitch, D.H., Michael, S.K., and McMahon, A.P. (1998). Modification of
1045 gene activity in mouse embryos in utero by a tamoxifen-inducible form of Cre recombinase. Curr Biol
1046 *8*, 1323-1326.

1047 Deries, M., Schweitzer, R., and Duxson, M.J. (2010). Developmental fate of the mammalian myotome.
1048 Developmental dynamics : an official publication of the American Association of Anatomists *239*,
1049 2898-2910.

1050 Diogo, R., Kelly, R.G., Christiaen, L., Levine, M., Ziermann, J.M., Molnar, J.L., Noden, D.M., and
1051 Tzahor, E. (2015). A new heart for a new head in vertebrate cardiopharyngeal evolution. Nature *520*,
1052 466-473.

1053 Duester, G. (2009). Keeping an eye on retinoic acid signaling during eye development. Chem Biol
1054 Interact *178*, 178-181.

Dupe, V., Matt, N., Garnier, J.M., Chambon, P., Mark, M., and Ghyselinck, N.B. (2003). A newborn lethal defect due to inactivation of retinaldehyde dehydrogenase type 3 is prevented by maternal retinoic acid treatment. Proceedings of the National Academy of Sciences of the United States of America *100*, 14036-14041.

Durand, J.P. (1976). Ocular development and involution in the European cave salamander, Proteus anguinus laurenti. Biol Bull *151*, 450-466.

Ericsson, R., Cerny, R., Falck, P., and Olsson, L. (2004). Role of cranial neural crest cells in visceral arch muscle positioning and morphogenesis in the Mexican axolotl, Ambystoma mexicanum. Developmental dynamics : an official publication of the American Association of Anatomists *231*, 237-247.

Evans, A.L., and Gage, P.J. (2005). Expression of the homeobox gene Pitx2 in neural crest is required for optic stalk and ocular anterior segment development. Human molecular genetics *14*, 3347-3359.

Eyal, S., Kult, S., Rubin, S., Krief, S., Felsenthal, N., Pineault, K.M., Leshkowitz, D., Salame, T.M., Addadi, Y., Wellik, D.M*., et al.* (2019). Bone morphology is regulated modularly by global and regional genetic programs. Development *146*.

Fogel, J.L., Thein, T.Z., and Mariani, F.V. (2012). Use of LysoTracker to detect programmed cell death in embryos and differentiating embryonic stem cells. J Vis Exp.

Franz-Odendaal, T.A., and Vickaryous, M.K. (2006). Skeletal elements in the vertebrate eye and adnexa: morphological and developmental perspectives. Developmental dynamics : an official publication of the American Association of Anatomists *235*, 1244-1255.

Gage, P.J., Rhoades, W., Prucka, S.K., and Hjalt, T. (2005). Fate maps of neural crest and mesoderm in the mammalian eye. Investigative ophthalmology & visual science *46*, 4200-4208.

Germain, P., Gaudon, C., Pogenberg, V., Sanglier, S., Van Dorsselaer, A., Royer, C.A., Lazar, M.A., Bourguet, W., and Gronemeyer, H. (2009). Differential action on coregulator interaction defines inverse retinoid agonists and neutral antagonists. Chem Biol *16*, 479-489.

Ghyselinck, N.B., Dupe, V., Dierich, A., Messaddeq, N., Garnier, J.M., Rochette-Egly, C., Chambon, P., and Mark, M. (1997). Role of the retinoic acid receptor beta (RARbeta) during mouse development. The International journal of developmental biology *41*, 425-447.

Gilbert, P. (1957). The origin and development of the human extrinsic ocular muscles. . Contrib Embryol, 36: 59-78.

Gilbert, P.W. (1947). The origin and development of the extrinsic ocular muscles in the domestic cat. Journal of morphology *81*, 151-193.

Gitton, Y., Heude, E., Vieux-Rochas, M., Benouaiche, L., Fontaine, A., Sato, T., Kurihara, Y., Kurihara, H., Couly, G., and Levi, G. (2010). Evolving maps in craniofacial development. Seminars in cell & developmental biology *21*, 301-308.

Grenier, J., Teillet, M.A., Grifone, R., Kelly, R.G., and Duprez, D. (2009). Relationship between neural crest cells and cranial mesoderm during head muscle development. PloS one *4*, e4381.

Grindley, J.C., Davidson, D.R., and Hill, R.E. (1995). The role of Pax-6 in eye and nasal development. Development *121*, 1433-1442.

Hagglund, A.C., Dahl, L., and Carlsson, L. (2011). Lhx2 is required for patterning and expansion of a distinct progenitor cell population committed to eye development. PloS one *6*, e23387.

Harding, P., and Moosajee, M. (2019). The Molecular Basis of Human Anophthalmia and Microphthalmia. J Dev Biol *7*.

Hasson, P. (2011). "Soft" tissue patterning: muscles and tendons of the limb take their form. Developmental dynamics : an official publication of the American Association of Anatomists *240*, 1100-1107.

Hasson, P., DeLaurier, A., Bennett, M., Grigorieva, E., Naiche, L.A., Papaioannou, V.E., Mohun, T.J., and Logan, M.P. (2010). Tbx4 and tbx5 acting in connective tissue are required for limb muscle and tendon patterning. Developmental cell *18*, 148-156.

Heude, E., Bellessort, B., Fontaine, A., Hamazaki, M., Treier, A.C., Treier, M., Levi, G., and Narboux-Neme, N. (2015). Etiology of craniofacial malformations in mouse models of blepharophimosis, ptosis and epicanthus inversus syndrome. Human molecular genetics *24*, 1670-1681.

Heude, E., Tesarova, M., Sefton, E.M., Jullian, E., Adachi, N., Grimaldi, A., Zikmund, T., Kaiser, J., Kardon, G., Kelly, R.G.*, et al.* (2018). Unique morphogenetic signatures define mammalian neck muscles and associated connective tissues. Elife *7*.

Huang, A.H. (2017). Coordinated development of the limb musculoskeletal system: Tendon and muscle patterning and integration with the skeleton. Developmental biology *429*, 420-428.

Huang, A.H., Riordan, T.J., Pryce, B., Weibel, J.L., Watson, S.S., Long, F., Lefebvre, V., Harfe, B.D., Stadler, H.S., Akiyama, H.*, et al.* (2015). Musculoskeletal integration at the wrist underlies the modular development of limb tendons. Development *142*, 2431-2441.

Iwata, J., Suzuki, A., Pelikan, R.C., Ho, T.V., and Chai, Y. (2013). Noncanonical transforming growth factor beta (TGFbeta) signaling in cranial neural crest cells causes tongue muscle developmental defects. The Journal of biological chemistry *288*, 29760-29770.

Jernvall, J., Aberg, T., Kettunen, P., Keranen, S., and Thesleff, I. (1998). The life history of an embryonic signaling center: BMP-4 induces p21 and is associated with apoptosis in the mouse tooth enamel knot. Development *125*, 161-169.

Johnston, M.C., Noden, D.M., Hazelton, R.D., Coulombre, J.L., and Coulombre, A.J. (1979). Origins of avian ocular and periocular tissues. Exp Eye Res *29*, 27-43.

Kardon, G. (1998). Muscle and tendon morphogenesis in the avian hind limb. Development *125*, 4019-4032.

Kardon, G., Harfe, B.D., and Tabin, C.J. (2003). A Tcf4-positive mesodermal population provides a prepattern for vertebrate limb muscle patterning. Developmental cell *5*, 937-944.

Kastner, P., Grondona, J.M., Mark, M., Gansmuller, A., LeMeur, M., Decimo, D., Vonesch, J.L., Dolle, P., and Chambon, P. (1994). Genetic analysis of RXR alpha developmental function: convergence of RXR and RAR signaling pathways in heart and eye morphogenesis. Cell *78*, 987-1003.

Kaucka, M., Petersen, J., Tesarova, M., Szarowska, B., Kastriti, M.E., Xie, M., Kicheva, A., Annusver, K., Kasper, M., Symmons, O.*, et al.* (2018). Signals from the brain and olfactory epithelium control shaping of the mammalian nasal capsule cartilage. Elife *7*.

Kaufman, M.H., Chang, H.H., and Shaw, J.P. (1995). Craniofacial abnormalities in homozygous Small eye (Sey/Sey) embryos and newborn mice. J Anat *186 (Pt 3)*, 607-617.

Kish, P.E., Bohnsack, B.L., Gallina, D., Kasprick, D.S., and Kahana, A. (2011). The eye as an organizer of craniofacial development. Genesis *49*, 222-230.

Lamb, T.D., Collin, S.P., and Pugh, E.N., Jr. (2007). Evolution of the vertebrate eye: opsins, photoreceptors, retina and eye cup. Nature reviews Neuroscience *8*, 960-976.

Langenberg, T., Kahana, A., Wszalek, J.A., and Halloran, M.C. (2008). The eye organizes neural crest cell migration. Developmental dynamics : an official publication of the American Association of Anatomists *237*, 1645-1652.

Li, L., Miano, J.M., Cserjesi, P., and Olson, E.N. (1996). SM22 alpha, a marker of adult smooth muscle, is expressed in multiple myogenic lineages during embryogenesis. Circulation research *78*, 188-195.

Li, Z., Marchand, P., Humbert, J., Babinet, C., and Paulin, D. (1993). Desmin sequence elements regulating skeletal muscle-specific expression in transgenic mice. Development *117*, 947-959.

Madisen, L., Zwingman, T.A., Sunkin, S.M., Oh, S.W., Zariwala, H.A., Gu, H., Ng, L.L., Palmiter, R.D., Hawrylycz, M.J., Jones, A.R.*, et al.* (2010). A robust and high-throughput Cre reporting and characterization system for the whole mouse brain. Nature neuroscience *13*, 133-140.

Matsuo, T., Osumi-Yamashita, N., Noji, S., Ohuchi, H., Koyama, E., Myokai, F., Matsuo, N., Taniguchi, S., Doi, H., Iseki, S.*, et al.* (1993). A mutation in the Pax-6 gene in rat small eye is associated with impaired migration of midbrain crest cells. Nature genetics *3*, 299-304.

1153 Matt, N., Dupe, V., Garnier, J.M., Dennefeld, C., Chambon, P., Mark, M., and Ghyselinck, N.B. (2005).
1154 Retinoic acid-dependent eye morphogenesis is orchestrated by neural crest cells. Development *132*,
1155 4789-4800.

1156 Matt, N., Ghyselinck, N.B., Pellerin, I., and Dupe, V. (2008). Impairing retinoic acid signalling in the
1157 neural crest cells is sufficient to alter entire eye morphogenesis. Developmental biology *320*, 140-148.

1158 McBratney-Owen, B., Iseki, S., Bamforth, S.D., Olsen, B.R., and Morriss-Kay, G.M. (2008).
1159 Development and tissue origins of the mammalian cranial base. Developmental biology *322*, 121-132.

1160 McGurk, P.D., Swartz, M.E., Chen, J.W., Galloway, J.L., and Eberhart, J.K. (2017). In vivo zebrafish
1161 morphogenesis shows Cyp26b1 promotes tendon condensation and musculoskeletal patterning in the
1162 embryonic jaw. PLoS genetics *13*, e1007112.

1163 Metscher, B.D. (2009). MicroCT for developmental biology: a versatile tool for high-contrast 3D
1164 imaging at histological resolutions. Developmental dynamics : an official publication of the American
1165 Association of Anatomists *238*, 632-640.

1166 Molotkov, A., Molotkova, N., and Duester, G. (2006). Retinoic acid guides eye morphogenetic
1167 movements via paracrine signaling but is unnecessary for retinal dorsoventral patterning.
1168 Development *133*, 1901-1910.

1169 Moreno, E., Valon, L., Levillayer, F., and Levayer, R. (2019). Competition for Space Induces Cell
1170 Elimination through Compaction-Driven ERK Downregulation. Curr Biol *29*, 23-34 e28.

1171 Mori, M., Ghyselinck, N.B., Chambon, P., and Mark, M. (2001). Systematic immunolocalization of
1172 retinoid receptors in developing and adult mouse eyes. Investigative ophthalmology & visual science
1173 *42*, 1312-1318.

1174 Mori-Akiyama, Y., Akiyama, H., Rowitch, D.H., and de Crombrugghe, B. (2003). Sox9 is required for
1175 determination of the chondrogenic cell lineage in the cranial neural crest. Proceedings of the National
1176 Academy of Sciences of the United States of America *100*, 9360-9365.

1177 Muzumdar, M.D., Tasic, B., Miyamichi, K., Li, L., and Luo, L. (2007). A global double-fluorescent Cre
1178 reporter mouse. Genesis *45*, 593-605.

1179 Nassari, S., Duprez, D., and Fournier-Thibault, C. (2017). Non-myogenic Contribution to Muscle
1180 Development and Homeostasis: The Role of Connective Tissues. Front Cell Dev Biol *5*, 22.

1181 Noden, D.M. (1983a). The embryonic origins of avian cephalic and cervical muscles and associated
1182 connective tissues. Am J Anat *168*, 257-276.

1183 Noden, D.M. (1983b). The role of the neural crest in patterning of avian cranial skeletal, connective,
1184 and muscle tissues. Developmental biology *96*, 144-165.

1185 Noden, D.M., and Francis-West, P. (2006). The differentiation and morphogenesis of craniofacial
1186 muscles. Developmental dynamics : an official publication of the American Association of Anatomists
1187 *235*, 1194-1218.

1188 Nonomura, K., Yamaguchi, Y., Hamachi, M., Koike, M., Uchiyama, Y., Nakazato, K., Mochizuki, A.,
1189 Sakaue-Sawano, A., Miyawaki, A., Yoshida, H.*, et al.* (2013). Local apoptosis modulates early
1190 mammalian brain development through the elimination of morphogen-producing cells. Developmental
1191 cell *27*, 621-634.

1192 Oh, S.P., Griffith, C.M., Hay, E.D., and Olsen, B.R. (1993). Tissue-specific expression of type XII
1193 collagen during mouse embryonic development. Developmental dynamics : an official publication of
1194 the American Association of Anatomists *196*, 37-46.

1195 Osumi-Yamashita, N., Ninomiya, Y., Doi, H., and Eto, K. (1994). The contribution of both forebrain and
1196 midbrain crest cells to the mesenchyme in the frontonasal mass of mouse embryos. Developmental
1197 biology *164*, 409-419.

1198 Pryce, B.A., Brent, A.E., Murchison, N.D., Tabin, C.J., and Schweitzer, R. (2007). Generation of
1199 transgenic tendon reporters, ScxGFP and ScxAP, using regulatory elements of the scleraxis gene.
1200 Developmental dynamics : an official publication of the American Association of Anatomists *236*,
1201 1677-1682.

1202 Rhinn, M., and Dolle, P. (2012). Retinoic acid signalling during development. Development *139*, 843-
1203 858.

Rhinn, M., Schuhbaur, B., Niederreither, K., and Dolle, P. (2011). Involvement of retinol dehydrogenase 10 in embryonic patterning and rescue of its loss of function by maternal retinaldehyde treatment. Proceedings of the National Academy of Sciences of the United States of America *108*, 16687-16692.

Rinon, A., Lazar, S., Marshall, H., Buchmann-Moller, S., Neufeld, A., Elhanany-Tamir, H., Taketo, M.M., Sommer, L., Krumlauf, R., and Tzahor, E. (2007). Cranial neural crest cells regulate head muscle patterning and differentiation during vertebrate embryogenesis. Development *134*, 3065-3075.

Roberts, R.C. (1967). Small eyes—a new dominant eye mutant in the mouse. Genet Res, Cam *9*, 121-122.

Rodriguez-Guzman, M., Montero, J.A., Santesteban, E., Ganan, Y., Macias, D., and Hurle, J.M. (2007). Tendon-muscle crosstalk controls muscle bellies morphogenesis, which is mediated by cell death and retinoic acid signaling. Developmental biology *302*, 267-280.

Rossant, J., Zirngibl, R., Cado, D., Shago, M., and Giguere, V. (1991). Expression of a retinoic acid response element-hsplacZ transgene defines specific domains of transcriptional activity during mouse embryogenesis. Genes & development *5*, 1333-1344.

Saga, Y., Miyagawa-Tomita, S., Takagi, A., Kitajima, S., Miyazaki, J., and Inoue, T. (1999). MesP1 is expressed in the heart precursor cells and required for the formation of a single heart tube. Development *126*, 3437-3447.

Sambasivan, R., Gayraud-Morel, B., Dumas, G., Cimper, C., Paisant, S., Kelly, R., and Tajbakhsh, S. (2009). Distinct regulatory cascades govern extraocular and pharyngeal arch muscle progenitor cell fates. Developmental cell *16*, 810-821.

Sambasivan, R., Kuratani, S., and Tajbakhsh, S. (2011). An eye on the head: the development and evolution of craniofacial muscles. Development *138*, 2401-2415.

Sandell, L.L., Sanderson, B.W., Moiseyev, G., Johnson, T., Mushegian, A., Young, K., Rey, J.P., Ma, J.X., Staehling-Hampton, K., and Trainor, P.A. (2007). RDH10 is essential for synthesis of embryonic retinoic acid and is required for limb, craniofacial, and organ development. Genes & development *21*, 1113-1124.

Sawtell, N.M., and Lessard, J.L. (1989). Cellular distribution of smooth muscle actins during mammalian embryogenesis: expression of the alpha-vascular but not the gamma-enteric isoform in differentiating striated myocytes. The Journal of cell biology *109*, 2929-2937.

Schweitzer, R., Chyung, J.H., Murtaugh, L.C., Brent, A.E., Rosen, V., Olson, E.N., Lassar, A., and Tabin, C.J. (2001). Analysis of the tendon cell fate using Scleraxis, a specific marker for tendons and ligaments. Development *128*, 3855-3866.

See, A.W., Kaiser, M.E., White, J.C., and Clagett-Dame, M. (2008). A nutritional model of late embryonic vitamin A deficiency produces defects in organogenesis at a high penetrance and reveals new roles for the vitamin in skeletal development. Developmental biology *316*, 171-190.

Sefton, E.M., and Kardon, G. (2019). Connecting muscle development, birth defects, and evolution: An essential role for muscle connective tissue. Current topics in developmental biology *132*, 137-176.

Serbedzija, G.N., Bronner-Fraser, M., and Fraser, S.E. (1992). Vital dye analysis of cranial neural crest cell migration in the mouse embryo. Development *116*, 297-307.

Shimizu, M., Narboux-Neme, N., Gitton, Y., de Lombares, C., Fontaine, A., Alfama, G., Kitazawa, T., Kawamura, Y., Heude, E., Marshall, L.*, et al.* (2018). Probing the origin of matching functional jaws: roles of Dlx5/6 in cranial neural crest cells. Scientific reports *8*, 14975.

Spencer, R.F., and Porter, J.D. (2006). Biological organization of the extraocular muscles. Progress in brain research *151*, 43-80.

Sugimoto, Y., Takimoto, A., Akiyama, H., Kist, R., Scherer, G., Nakamura, T., Hiraki, Y., and Shukunami, C. (2013). Scx+/Sox9+ progenitors contribute to the establishment of the junction between cartilage and tendon/ligament. Development *140*, 2280-2288.

Sulik, K.K., Dehart, D.B., Johnson, C.S., Ellis, S.L., Chen, S.Y., Dunty, W.C., Jr., and Zucker, R.M. (2001). Programmed cell death in extraocular muscle tendon/sclera precursors. Molecular vision *7*, 184-191.

1255 Suzuki, D.G., Fukumoto, Y., Yoshimura, M., Yamazaki, Y., Kosaka, J., Kuratani, S., and Wada, H.
1256 (2016). Comparative morphology and development of extra-ocular muscles in the lamprey and
1257 gnathostomes reveal the ancestral state and developmental patterns of the vertebrate head.
1258 Zoological Lett *2*, 10.

1259 Swinehart, I.T., Schlientz, A.J., Quintanilla, C.A., Mortlock, D.P., and Wellik, D.M. (2013). Hox11
1260 genes are required for regional patterning and integration of muscle, tendon and bone. Development
1261 *140*, 4574-4582.

1262 Tajbakhsh, S., Rocancourt, D., and Buckingham, M. (1996). Muscle progenitor cells failing to respond
1263 to positional cues adopt non-myogenic fates in myf-5 null mice. Nature *384*, 266-270.

1264 Thompson, H., Griffiths, J.S., Jeffery, G., and McGonnell, I.M. (2010). The retinal pigment epithelium
1265 of the eye regulates the development of scleral cartilage. Developmental biology *347*, 40-52.

1266 Tokita, M., and Schneider, R.A. (2009). Developmental origins of species-specific muscle pattern.
1267 Developmental biology *331*, 311-325.

1268 Twitty, V.C. (1932). Influence of the eye on the growth of its associated structures, studied by means
1269 of heteroplastic transplantation. Journal of Experimental Zoology *61*, 333-374.

1270 von Scheven, G., Alvares, L.E., Mootoosamy, R.C., and Dietrich, S. (2006). Neural tube derived
1271 signals and Fgf8 act antagonistically to specify eye versus mandibular arch muscles. Development
1272 *133*, 2731-2745.

1273 Williams, A.L., and Bohnsack, B.L. (2015). Neural crest derivatives in ocular development: discerning
1274 the eye of the storm. Birth defects research Part C, Embryo today : reviews *105*, 87-95.

1275 Yamamoto, Y., Stock, D.W., and Jeffery, W.R. (2004). Hedgehog signalling controls eye degeneration
1276 in blind cavefish. Nature *431*, 844-847.

1277 Yokomizo, T., Yamada-Inagawa, T., Yzaguirre, A.D., Chen, M.J., Speck, N.A., and Dzierzak, E.
1278 (2012). Whole-mount three-dimensional imaging of internally localized immunostained cells within
1279 mouse embryos. Nat Protoc *7*, 421-431.

1280 Young, G.C. (2008). Number and arrangement of extraocular muscles in primitive gnathostomes:
1281 evidence from extinct placoderm fishes. Biology letters *4*, 110-114.

1282 Zein, W.M., Lewanda, A.F., Traboulsi, E.I. and Jabs, E.W. (2012). Ocular Manifestations of
1283 Syndromes with Craniofacial Abnormalities. In Genetic Diseases of the Eye (2 ed) E.I. Traboulsi, ed.
1284 (Oxford University Press).

1285 Ziermann, J.M., Diogo, R., and Noden, D.M. (2018). Neural crest and the patterning of vertebrate
1286 craniofacial muscles. Genesis *56*, e23097.

1287 Zucker, R.M., Hunter, E.S., 3rd, and Rogers, J.M. (1999). Apoptosis and morphology in mouse
1288 embryos by confocal laser scanning microscopy. Methods *18*, 473-480.

1289

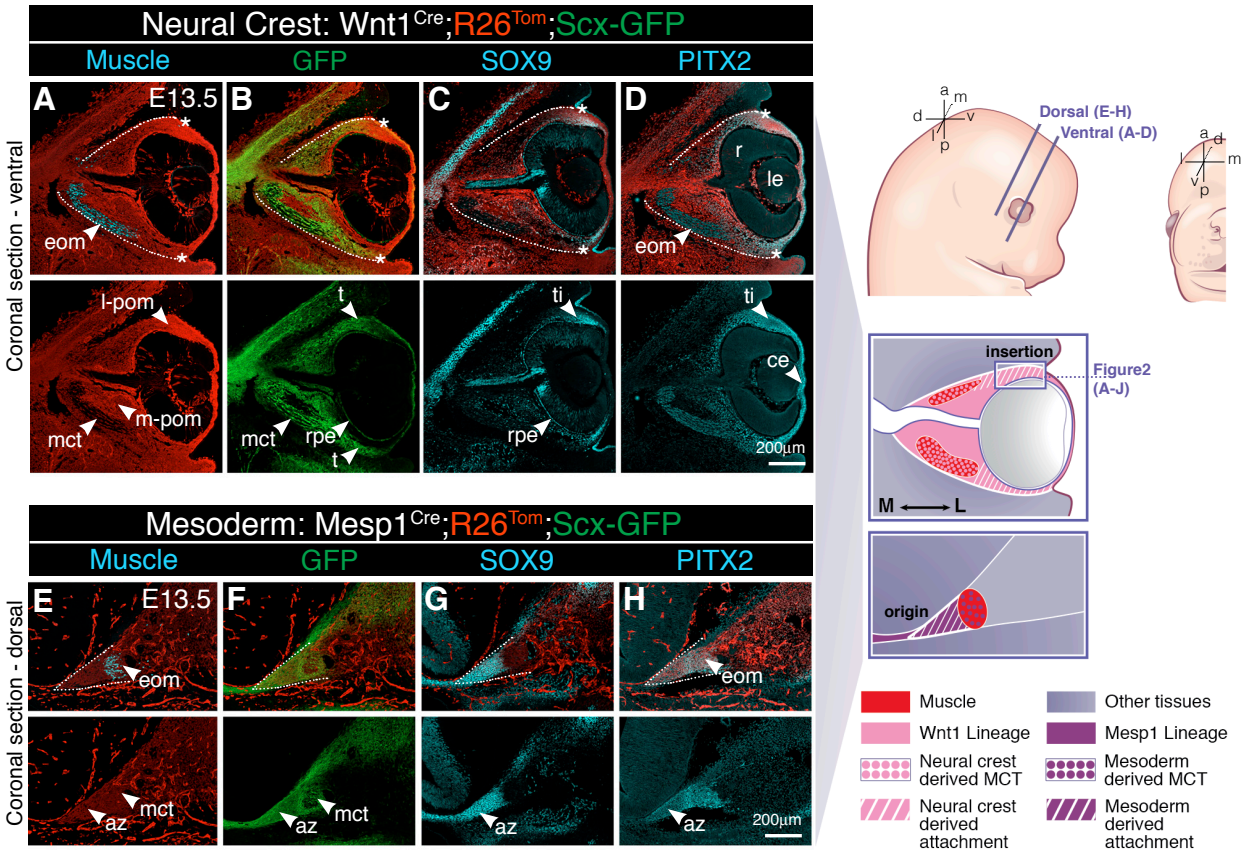
Neural Crest: Wnt1Cre;R26Tom;Scx-GFP
Muscle
GFP
SOX9
PITX2
A
E13.5
B
C
D
Coronal section - ventral
eom
r
le
l-pom
t
ti
ce
m-pom
mct
rpe
200µm
Mesoderm: Mesp1Cre;R26Tom;Scx-GFP
E
F
G
H
Coronal section - dorsal
az
Dorsal (E-H)
Ventral (A-D)
insertion
Figure2
(A-J)
M
L
origin
Muscle
Wnt1 Lineage
Neural crest derived MCT
Neural crest derived attachment
Other tissues
Mesp1 Lineage
Mesoderm derived MCT
Mesoderm derived attachment

Comai et al_Figure2

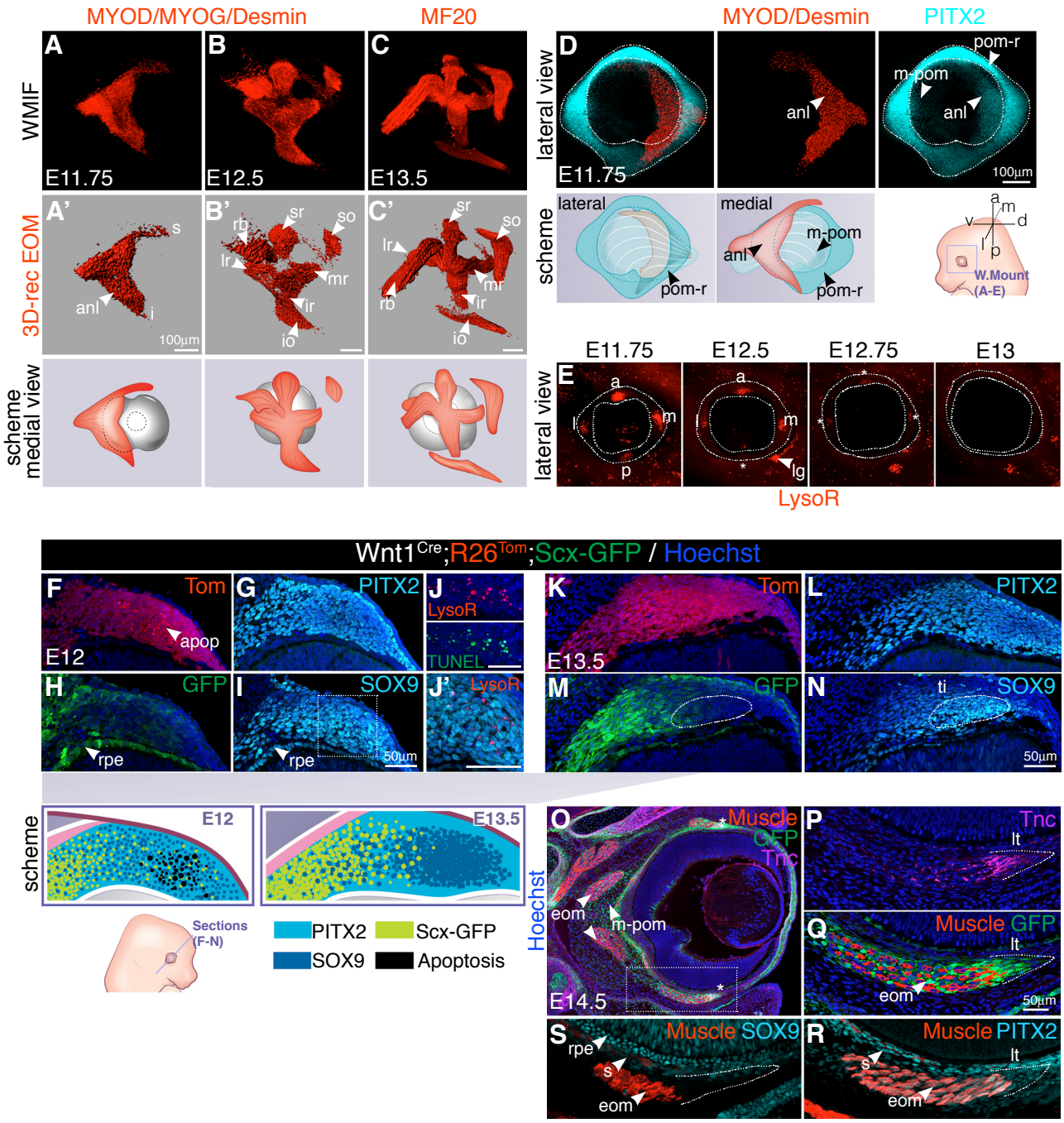

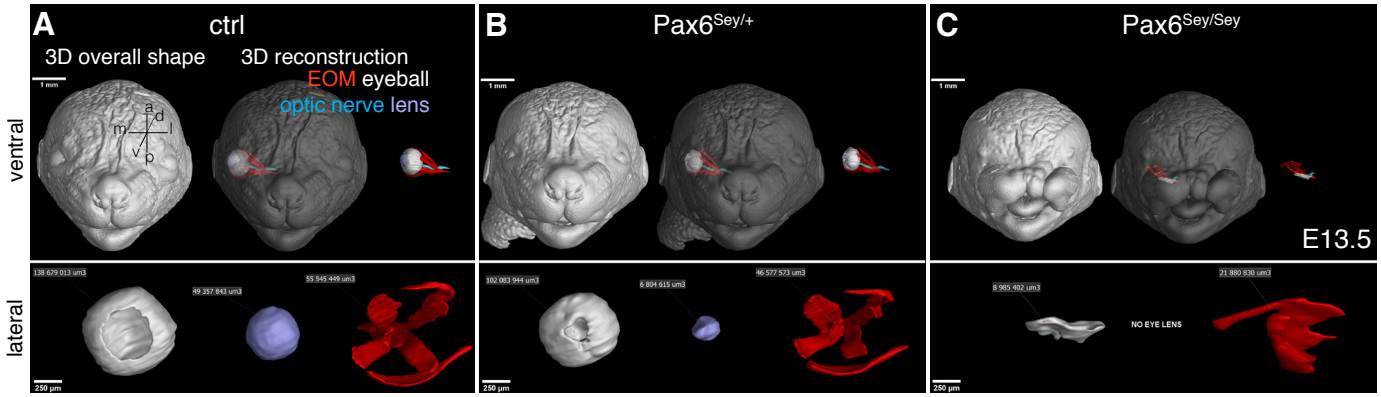
A
ctrl
3D overall shape
3D reconstruction
EOM eyeball
optic nerve lens
ventral
lateral
a
d
m
l
v
p
1 mm
250 µm
B
Pax6Sey/+
C
Pax6Sey/Sey
E13.5
NO EYE LENS

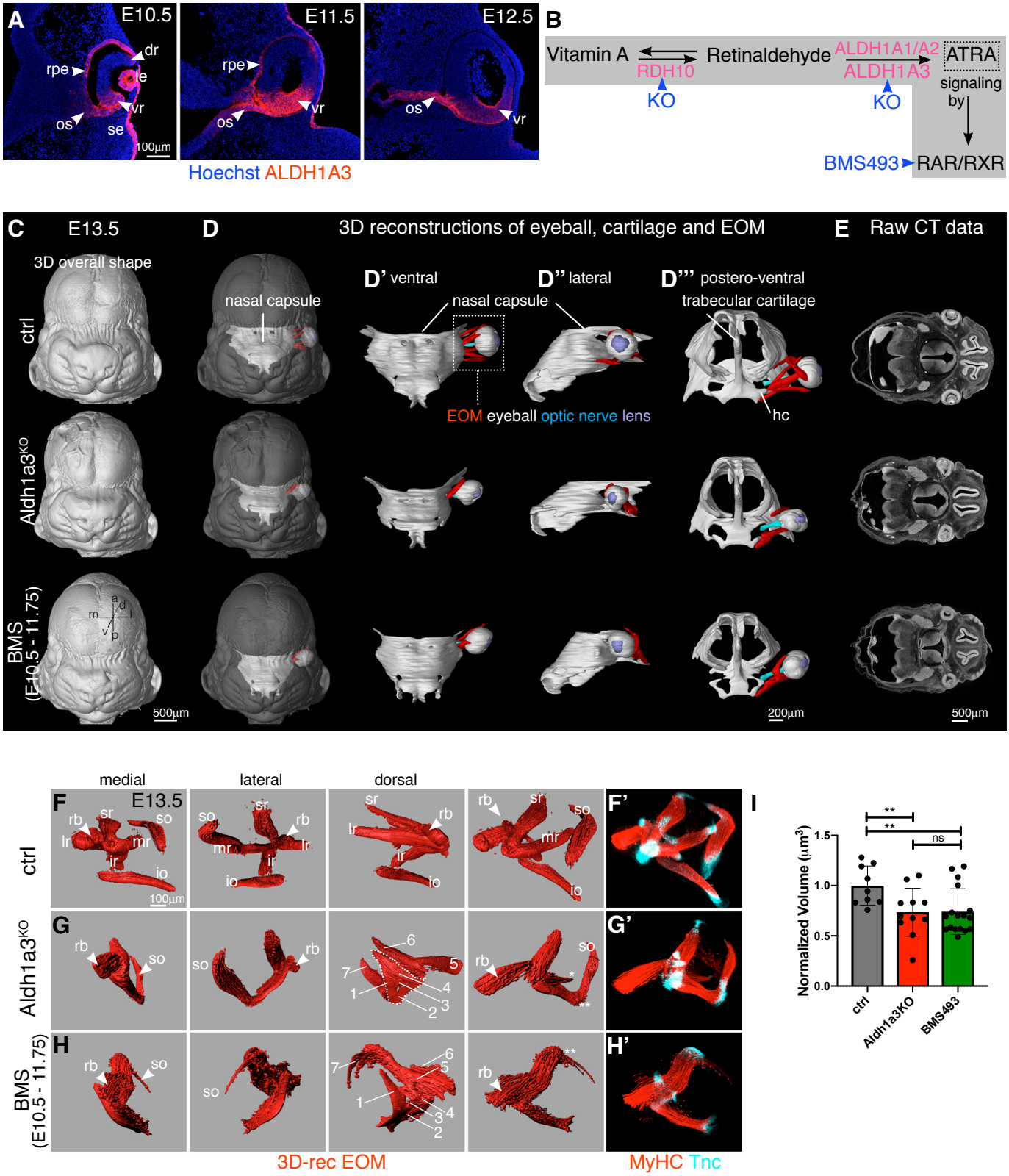
A
E10.5
E11.5
E12.5
dr
rpe
le
vr
os
se
100µm
Hoechst ALDH1A3
B
Vitamin A
Retinaldehyde
ALDH1A1/A2
ATRA
RDH10
ALDH1A3
KO
KO
signaling by
BMS493
RAR/RXR
C
E13.5
3D overall shape
D
3D reconstructions of eyeball, cartilage and EOM
E
Raw CT data
ctrl
Aldh1a3KO
BMS (E10.5 - 11.75)
nasal capsule
D' ventral
D'' lateral
D''' postero-ventral
trabecular cartilage
EOM eyeball optic nerve lens
hc
500µm
200µm
500µm
medial
lateral
dorsal
F
E13.5
rb
sr
so
lr
mr
ir
io
100µm
F'
G
G'
H
H'
3D-rec EOM
MyHC Tnc
I
Normalized Volume (µm3)
1.5
1.0
0.5
0.0
**
**
ns
ctrl
Aldh1a3KO
BMS493

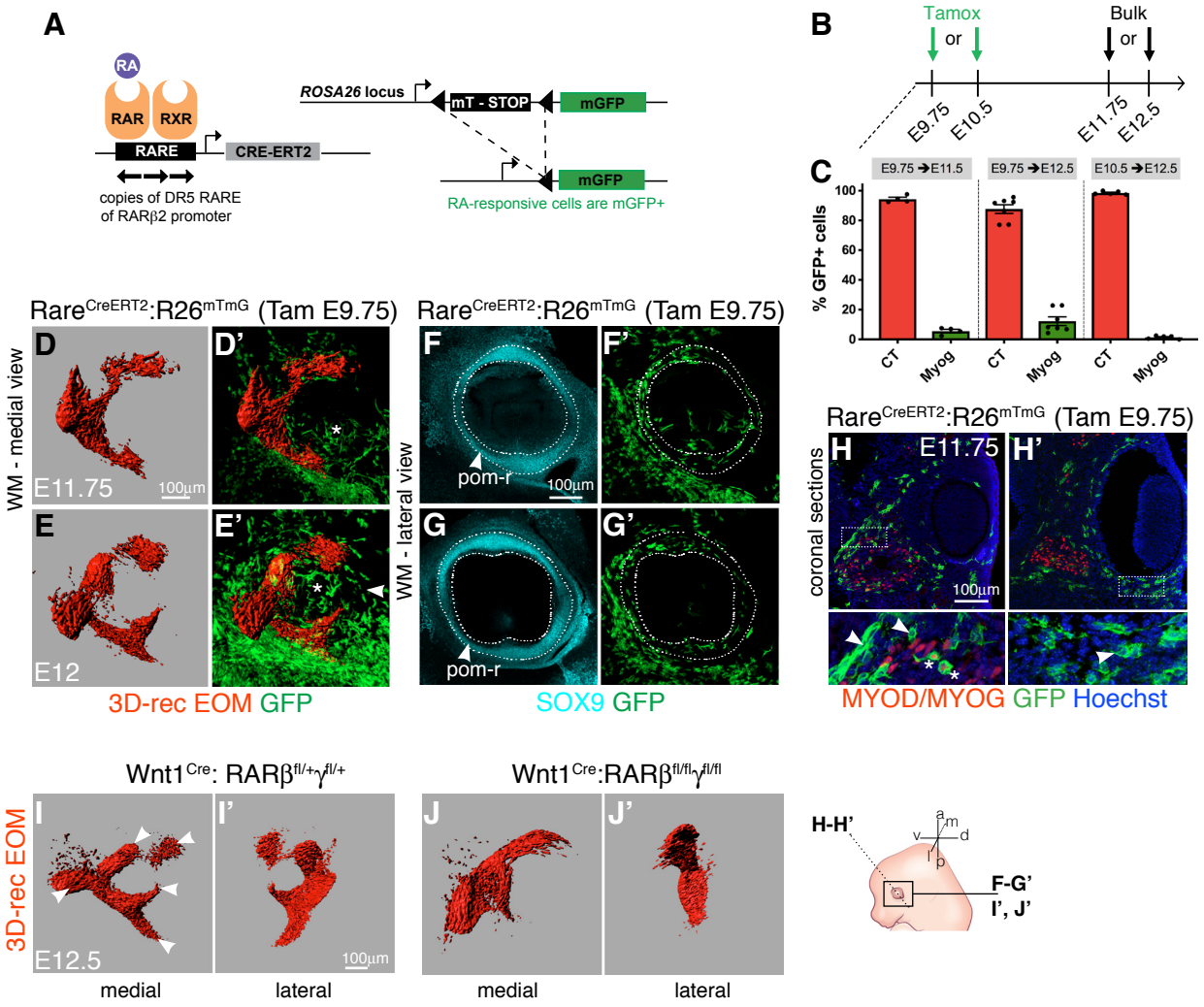
A
RA
RAR
RXR
RARE
CRE-ERT2
copies of DR5 RARE
of RARβ2 promoter
ROSA26 locus
mT - STOP
mGFP
mGFP
RA-responsive cells are mGFP+
B
Tamox
or
Bulk
or
E9.75
E10.5
E11.75
E12.5
C
E9.75 → E11.5
E9.75 → E12.5
E10.5 → E12.5
% GFP+ cells
100
80
60
40
20
0
CT
Myog
CT
Myog
CT
Myog
RareCreERT2:R26mTmG (Tam E9.75)
WM - medial view
D
D'
E11.75
100µm
E
E'
E12
3D-rec EOM GFP
RareCreERT2:R26mTmG (Tam E9.75)
WM - lateral view
F
F'
pom-r
100µm
G
G'
pom-r
SOX9 GFP
RareCreERT2:R26mTmG (Tam E9.75)
coronal sections
H
E11.75
H'
100µm
MYOD/MYOG GFP Hoechst
Wnt1Cre: RARβfl/+γfl/+
3D-rec EOM
I
I'
E12.5
100µm
medial
lateral
Wnt1Cre:RARβfl/flγfl/fl
J
J'
medial
lateral
H-H'
a
m
v
d
l
p
F-G'
I', J'

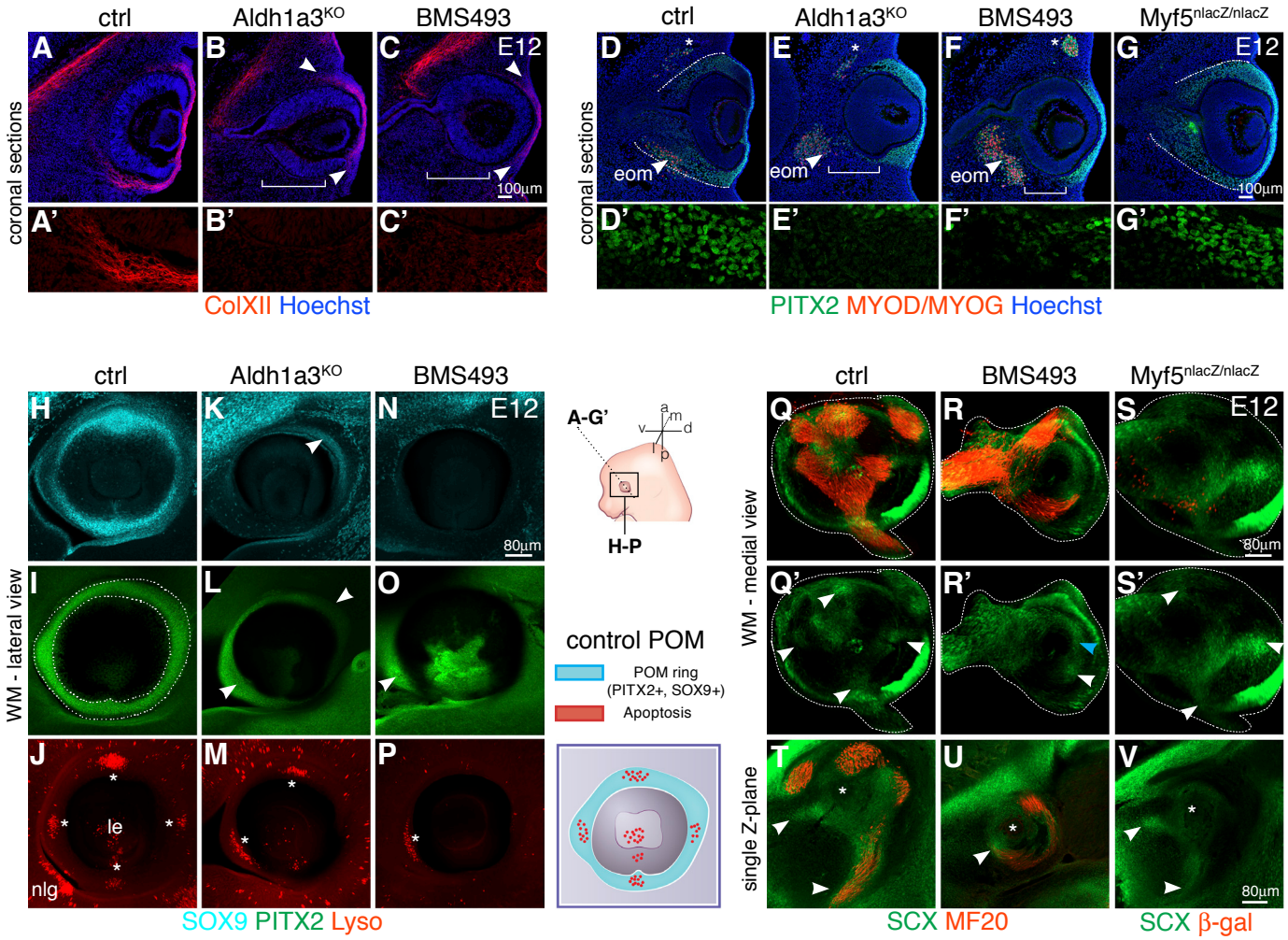
ctrl
Aldh1a3KO
BMS493
Myf5nlacZ/nlacZ
coronal sections
A
B
C
E12
100µm
A'
B'
C'
ColXII Hoechst
D
E
F
G
eom
D'
E'
F'
G'
PITX2 MYOD/MYOG Hoechst
H
K
N
80µm
WM - lateral view
I
L
O
J
M
P
le
nlg
SOX9 PITX2 Lyso
A-G'
a
m
v
d
l
p
H-P
control POM
POM ring
(PITX2+, SOX9+)
Apoptosis
WM - medial view
Q
R
S
Q'
R'
S'
single Z-plane
T
U
V
SCX MF20
SCX β-gal

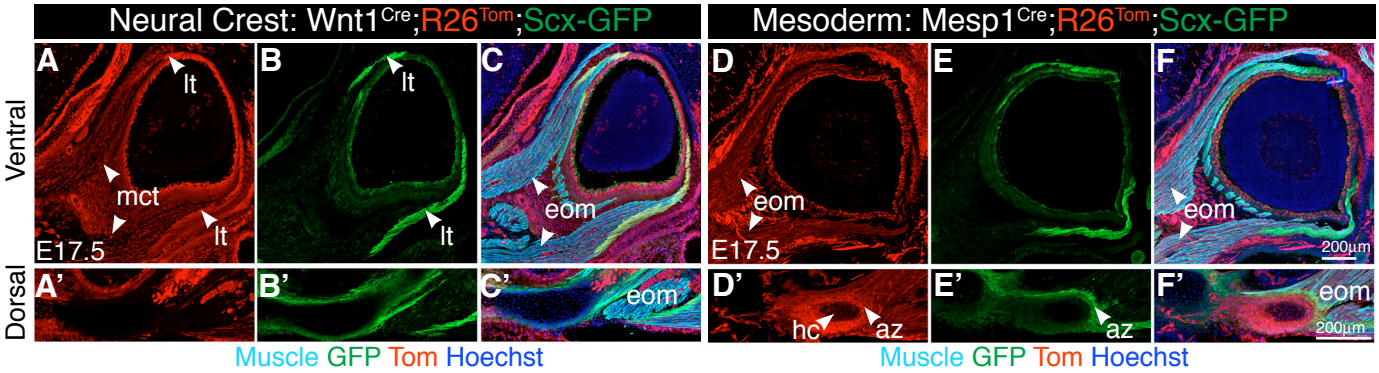
Neural Crest: Wnt1Cre;R26Tom;Scx-GFP
Mesoderm: Mesp1Cre;R26Tom;Scx-GFP
Ventral
Dorsal
A
B
C
D
E
F
A'
B'
C'
D'
E'
F'
lt
mct
eom
hc
az
E17.5
200µm
Muscle GFP Tom Hoechst
Muscle GFP Tom Hoechst

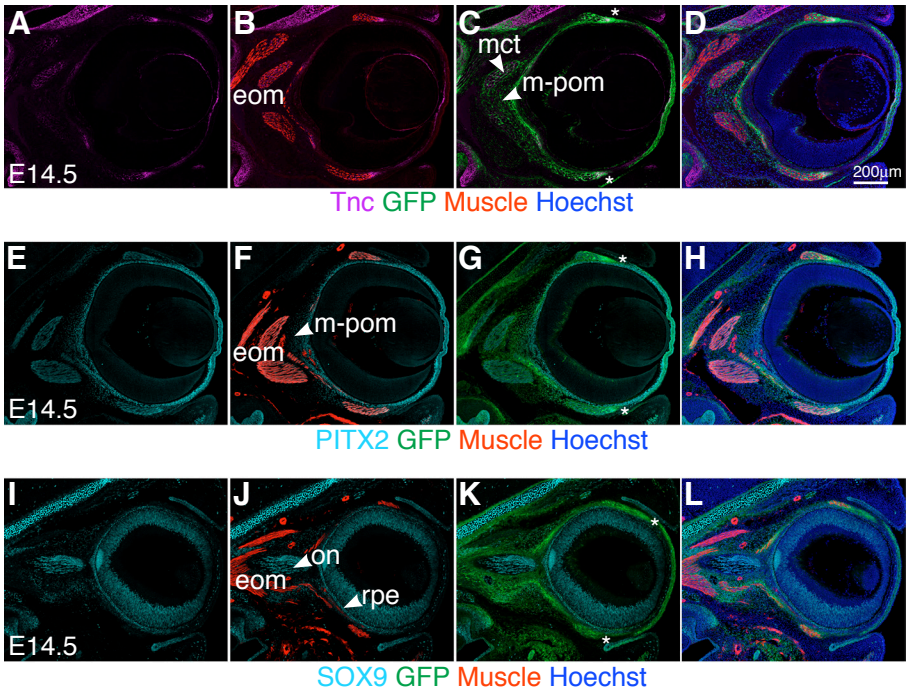
A
B
C
D
E14.5
eom
mct
m-pom
200µm
Tnc GFP Muscle Hoechst
E
F
G
H
E14.5
m-pom
eom
PITX2 GFP Muscle Hoechst
I
J
K
L
E14.5
on
eom
rpe
SOX9 GFP Muscle Hoechst

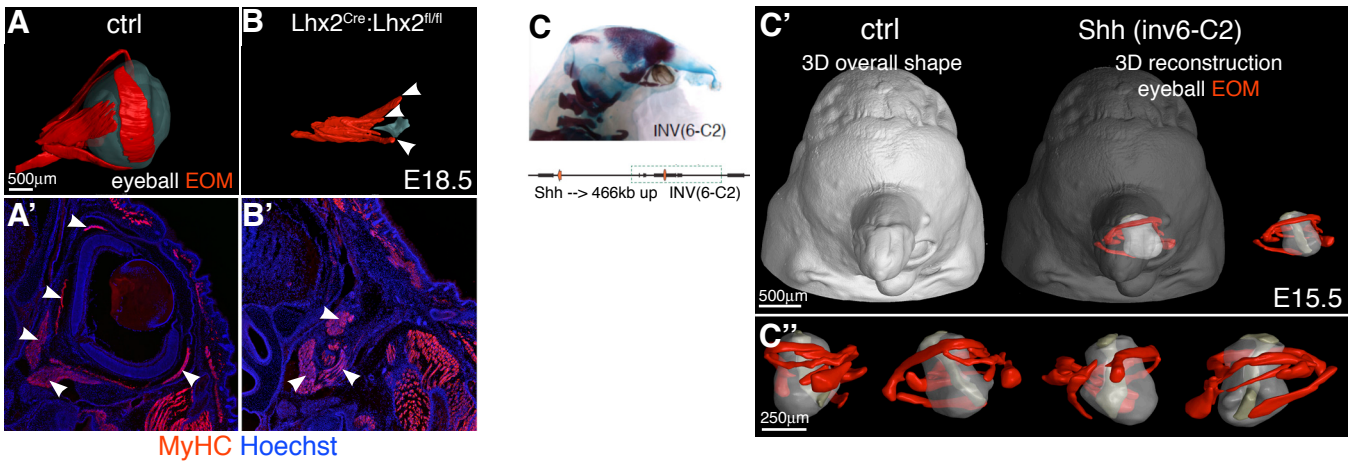
A
ctrl
B
Lhx2Cre:Lhx2fl/fl
500µm
eyeball EOM
E18.5
A'
B'
MyHC Hoechst
C
INV(6-C2)
Shh --> 466kb up
INV(6-C2)
C'
ctrl
3D overall shape
Shh (inv6-C2)
3D reconstruction
eyeball EOM
500µm
E15.5
C''
250µm

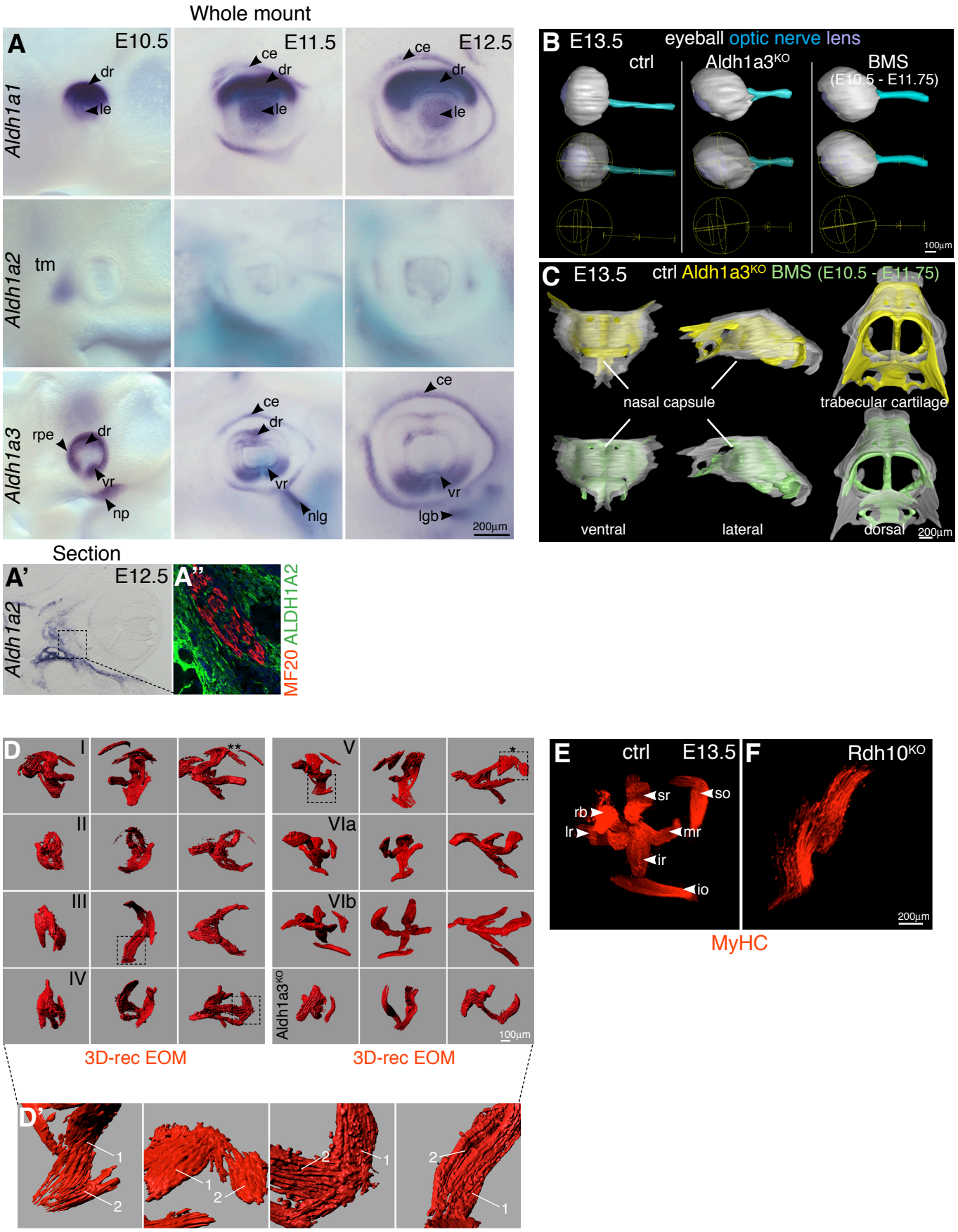
Whole mount
A
E10.5
E11.5
E12.5
Aldh1a1
Aldh1a2
Aldh1a3
dr
le
ce
tm
rpe
vr
np
nlg
lgb
200µm
B E13.5
eyeball optic nerve lens
ctrl
Aldh1a3KO
BMS
(E10.5 - E11.75)
100µm
C E13.5
ctrl Aldh1a3KO BMS (E10.5 - E11.75)
nasal capsule
trabecular cartilage
ventral
lateral
dorsal
200µm
Section
A'
E12.5
A''
MF20 ALDH1A2
D
I
II
III
IV
V
VIa
VIb
Aldh1a3KO
100µm
3D-rec EOM
3D-rec EOM
D'
1
2
E
ctrl
E13.5
sr
so
rb
lr
mr
ir
io
F
Rdh10KO
200µm
MyHC

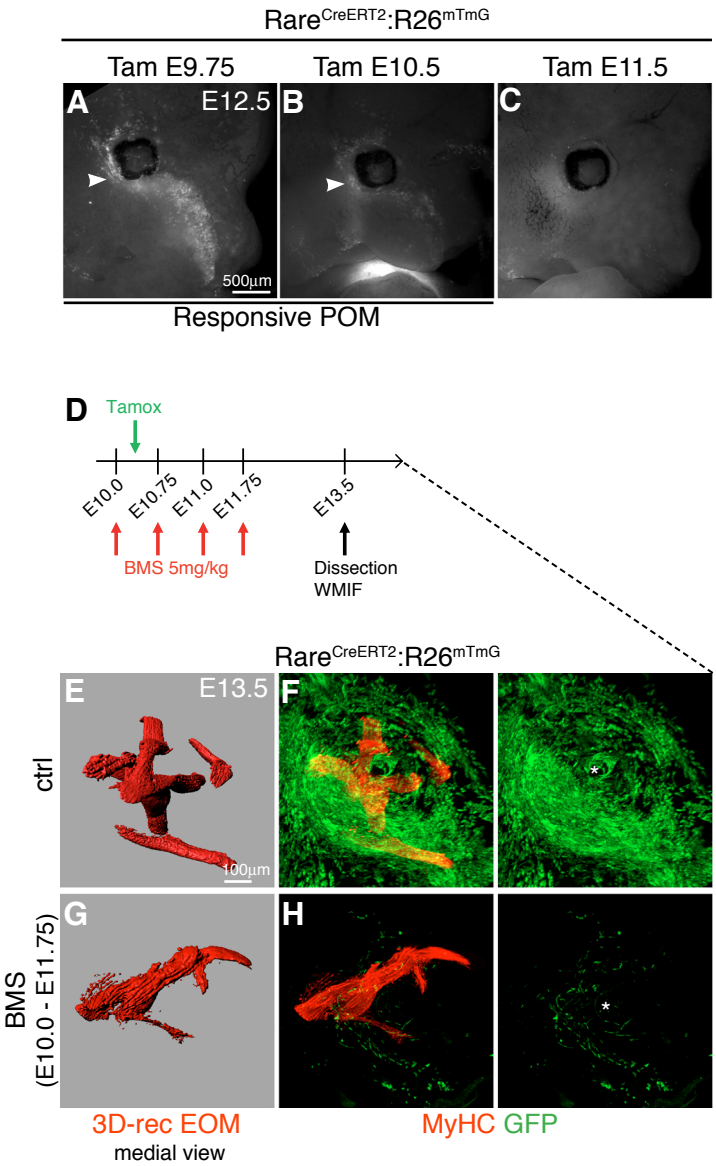
Rare^{CreERT2}:R26^{mTmG}
Tam E9.75
Tam E10.5
Tam E11.5
A
E12.5
B
C
500µm
Responsive POM
D
Tamox
E10.0
E10.75
E11.0
E11.75
E13.5
BMS 5mg/kg
Dissection
WMIF
Rare^{CreERT2}:R26^{mTmG}
E
E13.5
F
ctrl
100µm
G
H
BMS
(E10.0 - E11.75)
3D-rec EOM
medial view
MyHC GFP

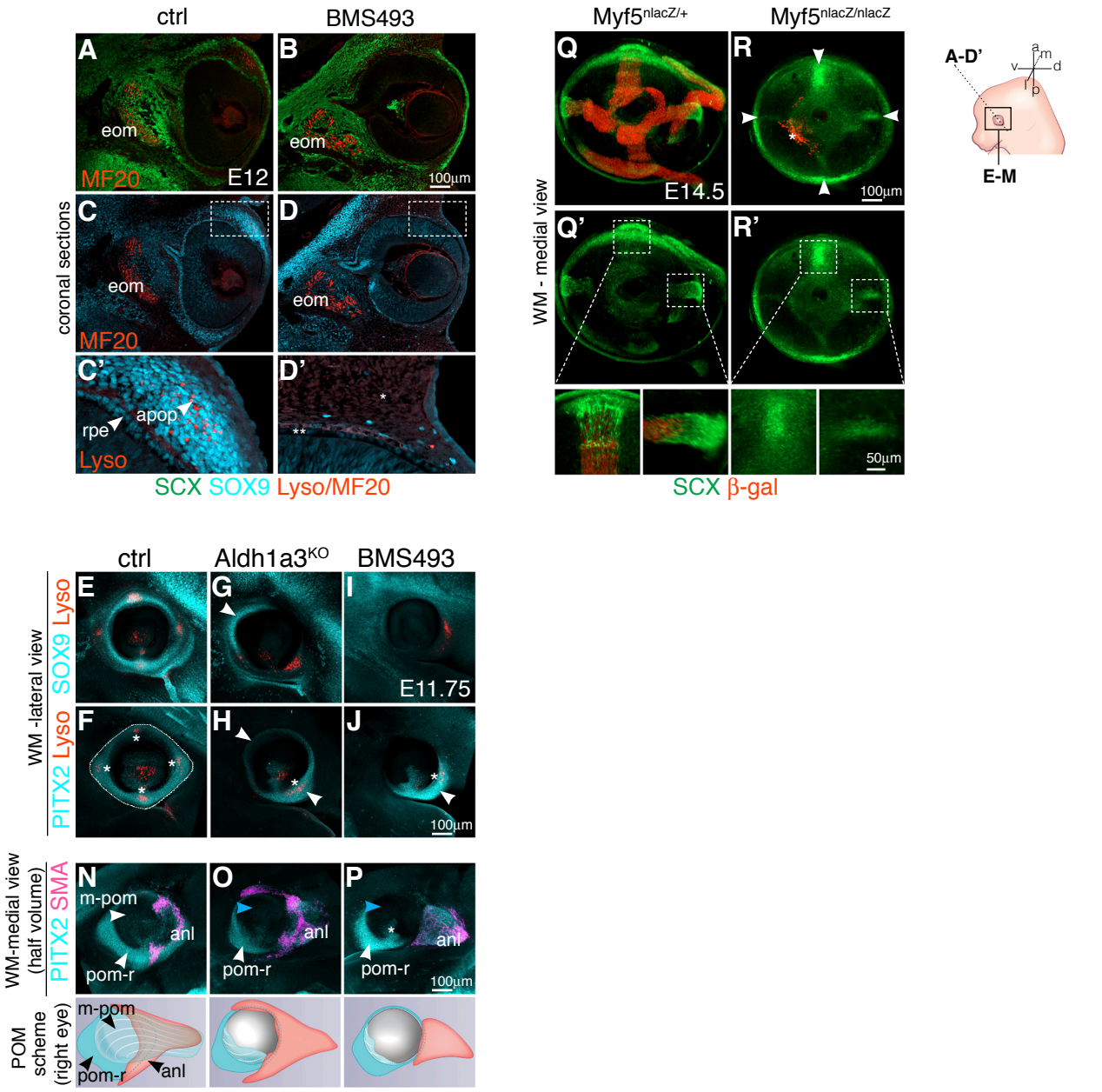
ctrl
BMS493
A
B
eom
MF20
E12
100µm
coronal sections
C
D
eom
MF20
C'
D'
rpe
apop
Lyso
SCX SOX9 Lyso/MF20
Myf5nlacZ/+
Myf5nlacZ/nlacZ
Q
R
E14.5
100µm
WM - medial view
Q'
R'
50µm
SCX β-gal
A-D'
a
m
v
d
l
p
E-M
ctrl
Aldh1a3KO
BMS493
WM -lateral view
PITX2 Lyso SOX9 Lyso
E
G
I
E11.75
F
H
J
100µm
WM-medial view (half volume)
PITX2 SMA
N
O
P
m-pom
anl
pom-r
100µm
POM scheme (right eye)

Table 1

Exp type	Conc BMS	Injections									Muscle phenotype (n° embryos)					N exp
		E10.5			E11.5			E12.5								
		mo	mid	eve	mo	mid	eve	mo	mid	eve	no	+	++	+++	n	
I	10 mg/Kg												3	3	6	4
II												1	7	1	9	2
III													4	5	9	2
IV												2	2		4	1
V											3	1	1		5	3
VI											2	3			5	1
														total	38	

Table2. Key Resources

REAGENT TYPE OR RESOURCE	DESIGNATION	SOURCE	Identifiers	Additional information
Primary antibody	Rabbit polyclonal anti-Aldh1A3	Sigma	Cat# HPA046271, RRID:AB_10965992	IF (1:100)/Citrate unmasking pH6
Primary antibody	Rabbit polyclonal anti-Aldh1A2	Abcam	Cat# ab96060, RRID:AB_10679336	IF (1:400)/Citrate unmasking pH6
Primary antibody	Chicken polyclonal anti-β-gal	Abcam	Cat. #: ab9361 RRID:AB_307210	IF (1:1000)
Primary antibody	Rabbit polyclonal anti-β-gal	MP Biomedicals	Cat. #: MP 559761 RRID:AB_2687418	IF (1:1500)
Primary antibody	Rabbit polyclonal anti-Collagen XII	from M. Koch	N/A	IF (1:3000)
Primary antibody	Mouse monoclonal IgG1 anti-Desmin	Dako	Cat# M0760, RRID:AB_2335684	IF (1:500)
Primary antibody	Chicken polyclonal anti-GFP	Abcam	Cat# ab13970, RRID:AB_300798	IF (1:1000)
Primary antibody	Rabbit polyclonal anti-GFP	Thermo Fisher Scientific	Cat# A-11122, RRID:AB_221569	IF (1:1000)
Primary antibody	Mouse monoclonal IgG1 anti-Myod	BD Biosciences	Cat# 554130, RRID:AB_395255	IF (1:100)
Primary antibody	Mouse monoclonal IgG1 anti-Myog	DSHB	Cat. #: F5D, RRID:AB_2146602	IF (1:30)
Primary antibody	Mouse monoclonal IgG2b anti-MF20	DSHB	Cat# MF 20, RRID:AB_2147781	IF (1:30)
Primary antibody	Rabbit polyclonal anti-MyHC	from G.Cossu	N/A	IF (1:750)
Primary antibody	Mouse monoclonal IgG1 anti-Pax7	DSHB	Cat. #: AB_528428, RRID:AB_528428	IF (1:20)
Primary antibody	Rabbit polyclonal anti-Pitx2	CapraScience	Cat# PA-1020, RRID:AB_2819162	IF (1:1000)
Primary antibody	Mouse monoclonal IgG2a anti-Smooth muscle actin-Cy3 conjugated	Sigma-Aldrich	Cat# C6198, RRID:AB_476856	IF (1:500)
Primary antibody	Rabbit polyclonal anti-Sox9	Millipore	Cat# AB5535, RRID:AB_2239761	IF (1:1500)
Primary antibody	Rat monoclonal IgG1 anti-Tenascin C	Thermo Fisher Scientific	Cat# MA1-26778, RRID:AB_2256026	IF (1:200)
Primary antibody	Mouse monoclonal IgG1 anti-Tnnt3	Sigma-Aldrich	Cat# T6277, RRID:AB_261723	IF (1:200)
Seconday antibody	Alexa Fluor® 633 Goat Anti-Chicken IgG (H+L)	Thermo Fisher Scientific	Cat# A-21103, RRID:AB_2535756	IF (1:500)
Seconday antibody	Alexa Fluor® 488 Goat Anti-Chicken IgG (H+L)	Thermo Fisher Scientific	Cat# A-11039, RRID:AB_2534096	IF (1:500)
Seconday antibody	Cy3 AffiniPure F(ab)'2 Fragment Donkey Anti-Chicken IgY (IgG)	Jackson ImmunoResearch Labs	Cat# 703-166-155, RRID:AB_2340364	IF (1:500)
Seconday antibody	Alexa Fluor® 488 AffiniPure F(ab')2 Fragment Donkey Anti-Chicken IgY (IgG)	Jackson ImmunoResearch Labs	Cat# 703-546-155, RRID:AB_2340376	IF (1:500)
Seconday antibody	Alexa Fluor® 633 F(ab')2 Fragment of Goat Anti-Rabbit IgG	Thermo Fisher Scientific	Cat# A-21072, RRID:AB_2535733	IF (1:500)
Seconday antibody	Alexa Fluor® 555 F(ab')2 Fragment of Goat Anti-Rabbit IgG	Thermo Fisher Scientific	Cat# A-21430, RRID:AB_2535851	IF (1:500)
Seconday antibody	Alexa Fluor® 488 F(ab')2 Fragment of Goat Anti-Rabbit IgG	Thermo Fisher Scientific	Cat# A-11070, RRID:AB_2534114	IF (1:500)
Seconday antibody	Alexa Fluor® 555 Goat Anti-Rat IgG (H+L)	Thermo Fisher Scientific	Cat# A-21434, RRID:AB_2535855	IF (1:500)
Seconday antibody	Alexa Fluor® 488 Goat Anti-Rat IgG (H+L)	Thermo Fisher Scientific	Cat# A-11006, RRID:AB_2534074	IF (1:500)
Seconday antibody	Alexa Fluor® 633 Goat Anti-Mouse IgG1(γ1)	Thermo Fisher Scientific	Cat# A-21126, RRID:AB_2535768	IF (1:500)
Seconday antibody	Cy3-AffiniPure Goat Anti-Mouse IgG1(γ1)	Jackson ImmunoResearch Labs	Cat# 115-165-205, RRID:AB_2338694	IF (1:500)
Seconday antibody	Alexa Fluor®488 AffiniPure Goat Anti-Mouse IgG1(γ1)	Jackson ImmunoResearch Labs	Cat# 115-545-205, RRID:AB_2338854	IF (1:500)
Seconday antibody	Alexa Fluor® 633 Goat Anti-Mouse IgG2b (γ2b)	Thermo Fisher Scientific	Cat# A-21146, RRID:AB_2535782	IF (1:500)
Seconday antibody	Cy3-AffiniPure Goat Anti-Mouse IgG2b (γ2b)	Jackson ImmunoResearch Labs	Cat# 115-165-207, RRID:AB_2338696	IF (1:500)
Seconday antibody	Alexa Fluor® 488 Goat Anti-Mouse IgG2b (γ2b)	Thermo Fisher Scientific	Cat# A-21141, RRID:AB_2535778	IF (1:500)
Chemical	Tamoxifen	Sigma-Aldrich	Cat#T5648	
Chemical	BMS493	Tocris	Cat#3509	
Commercial assay, kit	In Situ Cell Death Detection Kit - Fluorescein	Roche	Cat#11684795910	
Commercial assay, kit	LysoTracker™ Red DND-99	Thermo Fisher Scientific	Cat#L7528	
strain (*Mus musculus*)	B6D2F1/JRj	Janvier	N/A	
genetic reagent (*M. musculus*)	*R26^{mTmG}*	PMID:17868096	MGI:3716464	(Muzumdar et al., 2007)
genetic reagent (*M. musculus*)	*R26^{Tom} (Ai9)*	PMID:20023653	MGI:3809523	(Madisen et al., 2010)
genetic reagent (*M. musculus*)	*Mesp1Cre*	PMID:10393122	MGI:2176467	(Saga et al., 1999)
genetic reagent (*M. musculus*)	*Tg:Wnt1Cre*	PMID:9843687	MGI:2386570	(Danielian et al., 1998)
genetic reagent (*M. musculus*)	*Tg:Scx-GFP*	PMID:17497702	MGI:3717419	(Pryce et al., 2007)
genetic reagent (*M. musculus*)	*Myf5^{nlacZ}*		MGI:5581636	(Tajbakhsh et al., 1996)
genetic reagent (*M. musculus*)	*Aldh1a3^{KO}*	PMID:14623956	MGI:3043947	(Dupe et al., 2003)
genetic reagent (*M. musculus*)	*Rarb^{flox} (RARbetaL2)*	PMID:11857787	MGI:2386108	(Chapellier et al., 2002a)
genetic reagent (*M. musculus*)	*Rarg^{flox} (RARgammaL2)*	PMID:11857788	MGI:2386111	(Chapellier et al., 2002b)
genetic reagent (*M. musculus*)	*Rdh10^{KO} (Rdh10L-)*	PMID:21930923	MGI:5294926	(Rhinn et al., 2011)
genetic reagent (*M. musculus*)	*Pax6^{Sey}*	N/A	MGI:1856155	(Roberts, 1967)
genetic reagent (*M. musculus*)	*Lhx2^{Cre}*	PMID:21886788	MGI:5300954	(Hagglund et al., 2011)
	Lhx2^{flox}	PMID:20386748	MGI:4453328	(Tornqvist et al., 2010)